Six-Port Reflectometer Based Vector Network Analyzer with Two Independent RF Power Sources

Saif A. Aboud

A Thesis submitted to the Faculty of Graduate Studies of
The University of Manitoba in partial fulfillment of the requirement for
the degree of

Master of Science

Department of Electrical and Computer Engineering
University of Manitoba
Winnipeg, Manitoba, Canada

Abstract

This thesis presents a novel use of a six-port reflectometer (SPR) to build an SPR based network analyzer (SPNA) operating with two independent radio frequency (RF) power sources. The SPNA was first introduced by Hoer and Engen in the early 1970s using a common RF power source, along with power attenuators and a phase shifter. The basic description of a six-port reflectometer is having four side arms whose output is proportionally related to the incident voltage waves and the reflected ones at a measuring plane, i.e. measuring reflection coefficient of a device under testing (DUT) using only scalar power measurements at those four side arms. Throughout the research, a novel approach to the explicit calibration technique was developed apart from the traditional technique of using power measurements for several calibration standards, and the results confirmed its validity. Presented herein are the theory of SPR, calibration techniques, and SPNA, as well as simulated data which validate the main objective of this thesis. Physical realization of an SPR prototype for the chosen design, and results of the use of an arbitrarily DUT (Low Pass Filter – SLP 2400+) are presented in this report. Further work is required to confirm agreement between physical results of an SPNA with two independent RF power sources and the simulated.

Acknowledgements

I would like to take this opportunity to express my great appreciation to Dr. Joe LoVetri. Despite my demanding career as senior officer in the Royal Canadian Air Force, Dr. LoVetri was fully supportive of my part-time graduate studies and provided all support needed during my relocation to Ottawa, my year-long deployment to the Middle East, and assistance during COVID-19 travel restrictions. His supervision, support and guidance enabled me to complete my thesis objectives despite these challenges, and for that I'm indebted to him.

I would also like to thank Dr. Mohammed Asefi for his support, guidance, technical advice and other efforts that assisted me in building the prototype. His effort to have the circuit built while I was on deployment during an unprecedented times (COVID-19) is greatly appreciated and I am grateful for his assistance and his friendship. Special thank also go to Dr. Amer Zakaria, my friend, for his assistance when needed with MatLab algorithms.

I would like to thank all the technical staff within the Electrical and Computer Engineering department. Namely, Mr.James Dietrich for his assistance with acquiring and calibrating VNA for the physical measurements, Mr. Zoran Trajkoski for his technical assistance with building the physical circuit, Mr. Mount-first Ng for his technical support to enable me with remote access to ADS simulation, and finally to all CMC staff who assisted me throughout my graduate studies with ADS licensing and access.

I also extend my thanks to my M.Sc. committee, Dr. Greg Bridges and Dr. Dustin Isleifson, for taking their time to review and evaluate this thesis.

List of Contents

List of Figures

List of Tables

Chapter 1

Introduction

The purpose of this thesis is to investigate the feasibility for using a six-port reflectometer (SPR) as a six-port reflectometer based network analyzer (SPNA) operating with two independent oscillators to accurately measure scattering parameters (S-parameters) of a device under testing (DUT) in the low range of RF and microwave frequencies, specifically $1-2$ GHz. Other objectives such as low cost and small form were also set for this thesis.

1.1 Scattering Parameters

It has been shown in practice that at microwave frequencies, measurements of voltages and currents are not possible unless a clearly defined terminal pair is available. The terminal pair can be presented in a transverse electromagnetic (TEM) type line, such as a coaxial cable, microstrip and striplines, or non-TEM type lines, such as rectangular, circular or surface waveguide. To clearly define the terminal pair, this section will discuss briefly the concept of equivalent voltages and currents, as well as the linear relation between them demonstrated via impedance and admittance matrices. It will also introduce the scattering matrix, which is used to relate voltages and currents at microwave frequencies.

Consider two conductors in Figure 1, the total voltage from the positive conductor relative to the negative conductor can be calculated as

$$V = \int_{+}^{-} \overline{E}.\, d\bar{l} \tag{1.1}$$

and the total current can be determined by applying Ampere's law as

$$I = \oint_{C+} \overline{H}.\, d\bar{l} \tag{1.2}$$

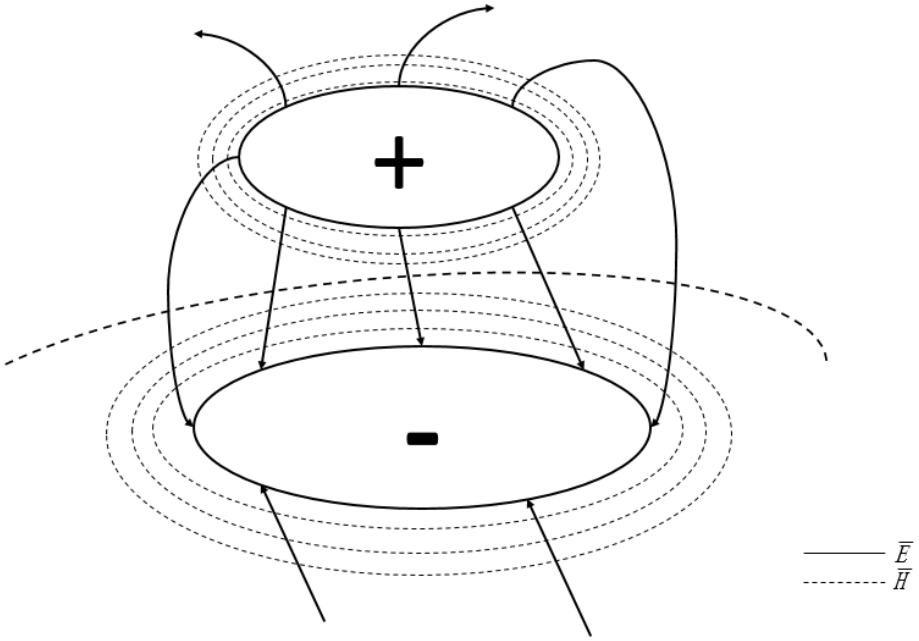

Figure 1.1: Electric and magnetic field lines for an arbitrary two-conductor TEM line

It is important to note that the total voltage (due to the electrostatic nature of the transverse fields between the two conductors) is unique and does not depend on the shape of the integration path [4]. Nonetheless, the total current depends on the integration of any closed path enclosing the positive conductor, but not the negative one. A characteristic impedance, Z_0, can be defined as

$$Z_0 = \frac{V}{I} \tag{1.3}$$

Now that we have defined total voltages, currents and characteristic impedance, and assuming we know the propagation constant for the line, we can apply circuit theory and analyze the line as a circuit element. However, the situation in the waveguide, non-TEM type, is more challenging to define. To explain why, consider Figure 2.

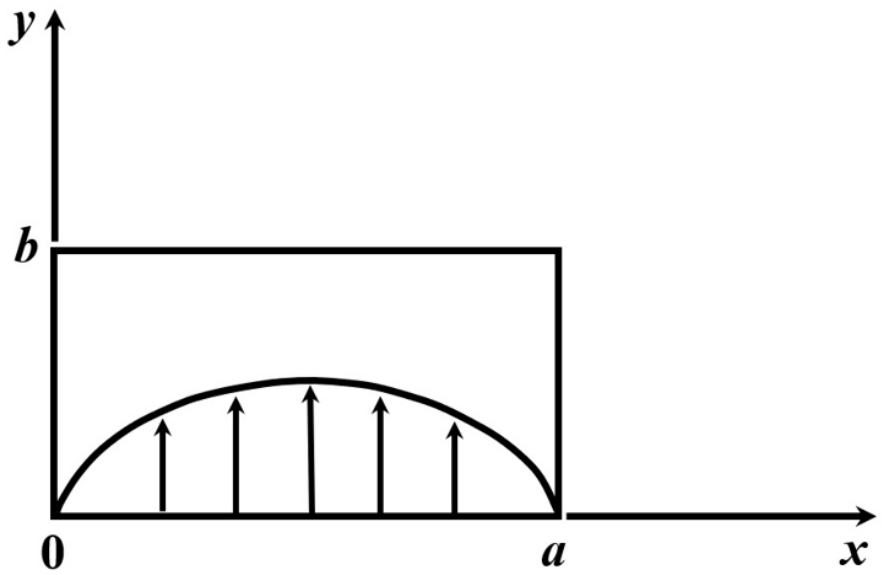

Figure 1.2: Electric field lines for TE_{10} mode of a rectangular waveguide

For the dominant TE_{10} mode, the transverse fields can be written as

$$E_y(x,y,z) = \frac{j\omega\mu a}{\pi} A sin\frac{\pi x}{a} e^{-j\beta z} = A e_y(x,y) e^{-j\beta z} \tag{1.4}$$

$$H_x(x,y,z) = \frac{j\beta a}{\pi} A sin\frac{\pi x}{a} e^{-j\beta z} = A h_x(x,y) e^{-j\beta z} \tag{1.5}$$

Applying (1.1) to the electric field in (4) gives

$$V = \frac{-j\omega\mu a}{\pi} A sin\frac{\pi x}{a} e^{-j\beta z} \int_y dy \tag{1.6}$$

where μ is the permeability of the waveguide, and β is the phase constant for TE_{10} mode.

From (1.6), the voltage depends on the position, x, and the integration contour along the y direction. This causes the voltage not to be unique, as the integration from $y = 0$ to b for $x = a/2$ gives a different voltage value than for integration from $y = 0$ to b for $x = 0$. The current and impedance also have the same problem. Therefore, to define equivalent voltages, currents and impedances that can be useful for non-TEM lines, we

need to consider the following:

- The voltages and currents are defined only for a particular waveguide mode and proportional to the electric field and the magnetic field respectively;
- The equivalent voltages and currents product gives the power flow of the waveguide mode; and
- The ratio of the voltage to the current for a single traveling wave are defined as the characteristic impedance for that mode.

then, for an arbitrary waveguide mode with both positive and negative traveling waves, the transverse fields can be written as

$$\overline{E}_t(x,y,z) = \overline{e}(x,y)(A^+e^{-j\beta z} + A^-e^{-j\beta z}) = \frac{\overline{e}(x,y)}{C_1}(V^+e^{-j\beta z} + V^-e^{-j\beta z}) \tag{1.7}$$

$$\overline{H}_t(x,y,z) = \overline{h}(x,y)(A^+e^{-j\beta z} + A^-e^{-j\beta z}) = \frac{\overline{h}(x,y)}{C_2}(I^+e^{-j\beta z} + I^-e^{-j\beta z}) \tag{1.8}$$

where $\overline{e}$ and $\overline{h}$ are transverse electric and magnetic field variations of the mode, and A^+ and A^- are the field amplitude of the traveling waves. Since $\overline{E_t}$ and $\overline{H_t}$ are related by the wave impedance,Z_w , we can relate $\overline{e}$ and $\overline{h}$ by

$$\overline{h}_t(x,y) = \frac{\hat{z} \times \overline{e}(x,y)}{Z_w} \tag{1.9}$$

Applying (1.1) and (1.2) to (1.7) and (1.8), we can define equivalent voltages and currents as

$$V(z) = V^+e^{-j\beta z} + V^-e^{-j\beta z} \tag{1.10}$$

$$I(z) = I^+e^{-j\beta z} - I^-e^{-j\beta z} \tag{1.11}$$

where $\frac{V^+}{I^+} = \frac{V^-}{I^-} = Z_0$.

This definition encompasses the idea of making the equivalent voltage and current proportional to the electric and magnetic fields, respectively. Through those definitions, we can utilize the impedance and/or admittance matrix concepts from circuit theory to relate those equivalent quantities at those various points, terminals or ports[1].

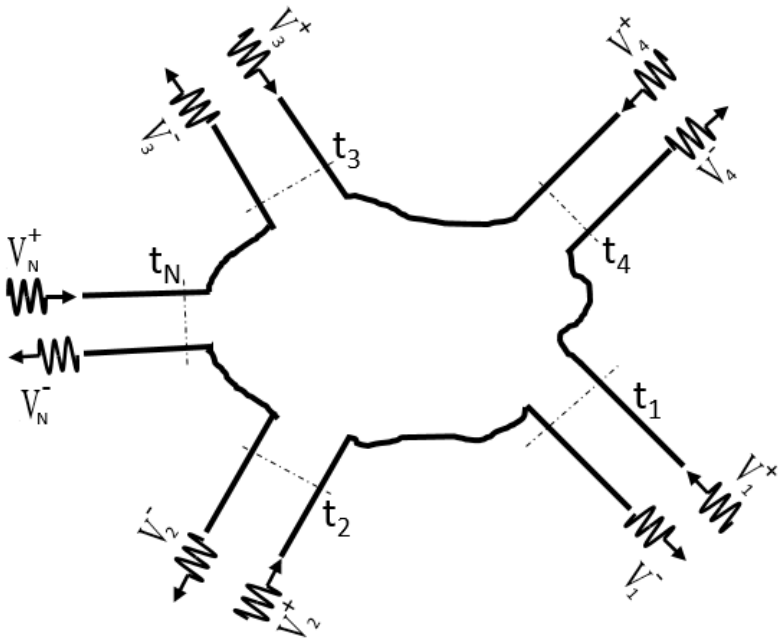

Figure 1.3: An arbitrary N-port microwave network

Consider the N-port network in Figure 3. The ports shown can be transmission line or waveguide, supporting any number of propagation modes. At a specific point of the n^{th} port, the terminal plane, t_N , is defined with the equivalent traveling wave voltages and currents for the incident and reflected waves, i.e. (V_n^+, I_n^+) and (V_n^-, I_n^-). The terminal planes are important for providing a phase reference for the voltages and currents that are complex-valued phasor quantities. At the n^{th} terminal plane, equations (1.10) and (1.11) become

$$V_n = V_n^+ + V_n^- \tag{1.12}$$

[1]The term port was first introduced by H.A Wheeler in the 1950s to replace a less descriptive term, "two-terminal pair" [4]

$$I_n = I_n^+ + I_n^- \tag{1.13}$$

The impedance matrix, [Z], linearly relates these voltages and currents

$$[V] = [Z][I] \tag{1.14}$$

and similarly, for an admittance matrix, [Y]

$$[I] = [Y][V] \tag{1.15}$$

Both impedance and admittance matrices linearly relate the total port voltages and currents. From (1.14) and (1.15), we note that

$$Z_{ij} = \left.\frac{V_i}{I_j}\right|_{I_k=0 \; for \; k\neq j} \tag{1.16}$$

$$Y_{ij} = \left.\frac{I_i}{V_j}\right|_{V_k=0 \; for \; k\neq j} \tag{1.17}$$

which means that Z_{ij} and Y_{ij} can be found by driving port j with current I_j, open-circuiting all ports and measuring voltage at port i, and with voltage V_j, short-circuiting all ports and measuring current at port i, respectively. Each of Z_{ij} and Y_{ij} elements can be complex. Network can be characterized as being reciprocal and lossy. Physically, networks that contain no active devices, nonreciprocal media such as ferrites, or plasmas can be characterized as reciprocal such as couplers and power dividers, and their impedance and admittance matrices are symmetric[4]. Impedance and/or admittance matrices are useful to identify those networks as reciprocal when $Z_{ij} = Z_{ji}$, $Y_{ij} = Y_{ji}$, and lossless where $Re\{Z_{mn}\}$ and/or $Re\{Y_{mn}\}$ are equal to zero, purely imaginary quantities.

For measurements at microwave frequencies, it is impossible to directly measure voltage and current quantities which are related to the electromagnetic field value on a fixed

specified plane; the quantities that are directly measured at microwave frequencies are standing-wave ratio, location of a field minima, and power. Another parameter that can be measured is the transmission coefficient through a circuit or port, which is a relative measurement of the amplitude and phase of the transmitted wave compared to the incident wave. Therefore, the measurable quantities are the amplitudes and phases of the waves reflected or scattered from a port [5]. The scattered waves are linearly related to the incident waves and the matrix that describes this linear relationship is called the scattering matrix.

The scattering matrix can provide a complete description to the network as seen at its N-port, such as the network's reciprocity and losslessness. While admittance and impedance matrices provide a linear relationship between voltages and currents, the scattering matrix provides a linear relationship between incident voltage wave and reflected voltage wave:

$$[V^-] = [S][V^+] \tag{1.18}$$

and like admittance and impedance elements, specific scattering matrix elements (S-parameters) can be determined as ratios of traveling wave voltages and currents. From (1.14) and (1.15), we note that

$$S_{ij} = \left.\frac{V_i^-}{V_j^+}\right|_{V_k^+=0 \; for \; k \neq j} \tag{1.19}$$

The scattering matrix is typically measured using vector network analyzer (VNA).

1.2 Vector Network Analyzer

The previous section introduced S-parameters and demonstrated how measurement can be done giving the challenges associated with those measurements at RF and microwave frequencies. This section will introduce the concept behind S-parameter measurement by a commercial VNA.

Different systems exist to measure reflection coefficients, S-parameters and to conduct network analysis measurements. These measuring systems can be categorized into scalar network analyzers (SNAs), which consist of directional couplers and measure amplitude property of a DUT at different frequencies, and vector network analyzers (VNAs), which are more accurate and can measure amplitude and phase; they are also capable of error corrections. VNAs are widely used to measure S-parameters of microwave networks such as amplifiers, filters, or any DUT of a N-port network, over an extensive range of frequencies. VNAs are complex to design, since – in addition to the display, storage and computation features, they provide an in situ vector error correction for verity of measurements at a wide range of frequencies. VNA design complexity makes them expensive, and in some cases —depending on the size of a DUT and the testing environment— they are not practical; therefore, they are mostly located within controlled environments or laboratories. VNAs require coaxial cables at their measuring planes to conduct measurements. The length of these cables can vary with the size of a DUT, thus, they can contribute to the complexity of calibration procedure setup (systematic errors), as well as the cost of the procedure [3].

As the features and measurement options of commercial VNA's increase, the complexity of the VNA increases. Additionally, the required procedures to calibrate DC biasing, DC contact resistance and errors —whether systematic (due to imperfections in design and test setup), random (mainly due to noise, or switching connectors repeatability) or drift (mainly caused by temperature variation)— will be more complex [7, 8]. This increase in complexity also corresponds to an increase in the use of microwave components and electrical circuitry, which contribute to the size and weight of the VNA, as well as the complexity of the firmware required to integrate these components to operate as desired. It is important to note that an increase in complexity results in an increase in cost; a two-port VNA can be a fraction of the price of a four-port or eight-port VNA.

Increases in the microwave and electrical components make the VNA expensive and

heavy and limit its use to labs and controlled environments. This makes VNAs inflexible and impractical for users to conduct measurements outside these environments (e.g. in one of the applications areas of interest here, imaging of stored-grain withing grain-bins [6]), whereas the use of a six-port reflectometer as a tool to conduct S-parameters measurements can offer the simplicity and flexibility users are seeking. There are, however, trade-offs to be considered for this simplicity; there are limitations to what a six-port reflectometer as VNA can offer (i.e. S-parameters measurements versus the S-parameters, response time and internal error corrections commercial VNAs can offer). In addition to the measuring options, commercial VNA calibration tends to be not as lengthy as that required for six-port reflectometers, though six-port reflectometers need only to be calibrated once. This will be explained in later chapters.

1.3 Motivation, Goals and Scope

The main objective of this thesis is to investigate the feasibility of implementing an SPNA operating with separate and independent RF power sources to provide accurate S-parameter measurements for a two-port network DUT. This will provide the practicality for the SPNA to be used for any size DUT, in any environment, with minimal impact on the length of the measuring coaxial cables and cost. In addition to the feasibility of operation using independent oscillators, the SPNA would be required to operate with wide bandwidth at low range RF and microwave frequencies, $1 - 2$ GHz.

With the main objective in mind, the research focused on SPR theory, models, designs, and calibration techniques. The theory of an SPR provided two models, linear and quadratic; this thesis focused on the latter. Many designs for SPR quadratic models were investigated and the *Frequency compensated quasi-optimal* design was chosen for this thesis [12 – 22]. The design consists of four $3dB$ Hybrid 90° couplers and a Wilkinson's power divider, which can be realized using microwave integrated circuits operating over a

reasonably wide bandwidth, while ensuring the circuit's small size for the practicality and flexibility required for this thesis.

Many SPR calibration techniques have been investigated to measure accurate reflection coefficient of a DUT. Most of these techniques are based on accurate SPR scalar power measurements, however, they vary with the number of calibration standards to be used and the algorithm complexity to compute the SPR's 11 calibration factors [12, 23 – 30]. This thesis makes use of the SPR theory to implement a novel and intuitive approach for calibrating an SPR by simply measuring the 6x6 S-parameters for the SPR circuit using a VNA, computing the 11 calibration factors required, and storing their values for future operation of the SPR.

To confirm this thesis research, Keysight Advanced Design System (ADS) 2019 update 1 was utilized to simulate the chosen design, measure its S-parameters for the 11 calibration factors, as well as design some arbitrary one-port and two-port networks as DUTs. The algorithm for computing the calibration factors and results was derived from SPR and SPNA theory and implemented using MathWorks MatLab.

1.4 Overview

Chapter 2 begins with a brief history of SPRs and describes the theory behind SPRs. This includes the mathematical derivation of the equations describing the relationship between measured power at the power detectors and the reflection coefficient at the measuring plane. The chapter also presents graphical interpretations of the theory and compares the graphical representation of six and five-port reflectometers. Finally, chapter 2 discusses some of the designs of SPRs and analysis of the chosen design.

Chapter 3 presents the most common calibration techniques and briefly highlights the use of many calibration standards. It also discusses the novel calibration approach which is

specific to the chosen design, as well as presenting simulation results and analysis.

Chapter 4 discusses the theory of SPNAs and presents and validates an SPNA with independent RF power sources results in comparison to Hoer's original design (common oscillator).

Chapter 5 presents the physical realization and implementation of the prototype, including all the parameters and components used to build it, as well as results.

Chapter 6 concludes and summarizes this thesis, provides guidance on future work to improve the prototype and, consequently, the results.

Chapter 2

Six-Port Reflectometer

This chapter introduces the history of the six-port reflectometer, the theory of operation, graphical interpretation, structure and design of six-port reflectometers, as well as the topology and design of the chosen prototype. Advantages of choosing a six-port reflectometer (versus five-port or four-port) will also be discussed in this chapter.

2.1 History of six-port reflectometers

In the early 1970s, work by C. Hoer and G.F. Engen at the National Bureau of Standards on designing broadband very high frequency (VHF) directional couplers led to a new and simple approach to measure voltages, currents, power, complex impedance and phase angle using a six-port passive coupler [1]. This coupler gave these measurements from power or voltage magnitudes measured from its four side-arms. The six-port coupler was designed using transmission lines and waveguides, hence designs solely requires one to conduct measurements of power and voltages in high frequency ranges. As microwave circuit design technologies (microwave integrated circuit (MIC), and monolithic MIC (MMIC)) progressed, six-port couplers (later called six-port reflectometers) became more practical and feasible to measure power and voltage magnitudes in the RF and microwave frequency ranges. The low cost and simple design of the six-port reflectometer made it desirable in many applications (such as low-cost digital receivers) due to low power consumption in wireless devices, measurement of S-parameters of DUT in microwave applications, and to realize low-cost for high-performance radar in automobile industries [9, 10, 11].

2.2 Theory

Six-port reflectometers are generally made of six passive ports, four of which are fitted permanently with power detectors (D3, D4, D5 and D6), with one port connected to a main oscillator and one to the DUT's measurement plane. The internal circuitry of the six-port reflectometer consists of passive lines (T-lines, microstrip or stripline) connecting power dividers and couplers or other MICs and electronics. The main advantage of the six-port reflectometer is its capability to measure complex S-parameters of a DUT using scalar measurements of power levels at the power detectors. It is noted that no phase measurement is required, hence simplifying the required measurements.

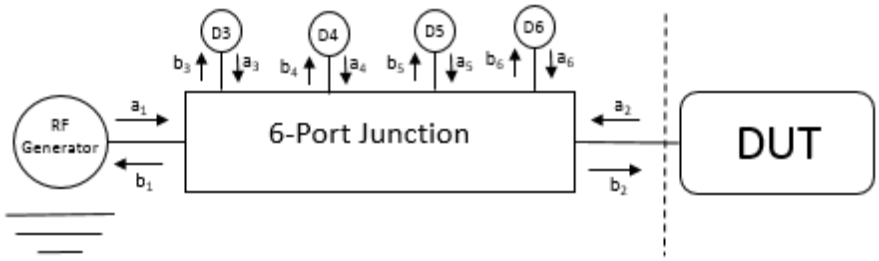

Figure 2.1: Basic six-port reflectometer

To analyze the six-port reflectometer, from Figure 2.1 and looking from outside the six-port junction, the scattering parameters relates the incident traveling voltage waves (V^+), a_i, and the reflected traveling voltage waves(V^-), b_i,

$$[b] = [S][a] \tag{2.1}$$

where $[S]$ is a 6x6 matrix, and $i = 1, 2, 3, 4, 5$ and 6. To determine the values for [S], let the reflection coefficient for D at each port i, where $i = 3, 4, 5$, and 6 be

$$\Gamma_i = \frac{a_i}{b_i} \tag{2.2}$$

Using (2.1) and (2.2), we can determine the $[\bar{S}]$ (depends on what is connected to ports 3, 4, 5, and 6) to be [12]:

$$\begin{bmatrix} b_1 \\ b_2 \\ 0 \\ 0 \\ 0 \\ 0 \end{bmatrix} = \begin{bmatrix} S_{11} & S_{12} & S_{13}\Gamma_3 & S_{14}\Gamma_4 & S_{15}\Gamma_5 & S_{16}\Gamma_6 \\ S_{21} & S_{22} & S_{23}\Gamma_3 & S_{24}\Gamma_4 & S_{25}\Gamma_5 & S_{26}\Gamma_6 \\ S_{31} & S_{32} & (S_{33}\Gamma_3 - 1) & S_{34}\Gamma_4 & S_{35}\Gamma_5 & S_{36}\Gamma_6 \\ S_{41} & S_{42} & S_{43}\Gamma_3 & (S_{44}\Gamma_4 - 1) & S_{45}\Gamma_5 & S_{46}\Gamma_6 \\ S_{51} & S_{52} & S_{53}\Gamma_3 & S_{54}\Gamma_4 & (S_{55}\Gamma_5 - 1) & S_{56}\Gamma_6 \\ S_{61} & S_{62} & S_{63}\Gamma_3 & S_{64}\Gamma_4 & S_{65}\Gamma_5 & (S_{66}\Gamma_6 - 1) \end{bmatrix} \begin{bmatrix} a_1 \\ a_2 \\ b_3 \\ b_4 \\ b_5 \\ b_6 \end{bmatrix} \tag{2.3}$$

The general solution for a_1, a_2 and b_i, from (2.3) is

$$a_1 = m_{11}b_1 + m_{12}b_2 \tag{2.4}$$

$$a_2 = m_{21}b_1 + m_{22}b_2 \tag{2.5}$$

$$b_i = m_{i1}b_1 + m_{i2}b_2 \tag{2.6}$$

where $i = 3, 4, 5,$ and 6, and m_{ij} are the elements of inverse matrix in (2.3), $[\bar{S}]^{-1}$. The reflection coefficient at the DUT is

$$\Gamma_{DUT} = \frac{a_2}{b_2} \tag{2.7}$$

Thus, solving (2.4) and (2.5) for b_1, and substitute in (2.6) with (2.7), b_i becomes:

$$b_i = \frac{m_{i1}}{m_{21}}\left(\frac{m_{i2}m_{21}}{m_{i1}} - m_{22} + \Gamma_{DUT}\right)b_2 \tag{2.8}$$

and letting $A_i = \frac{m_{i1}}{m_{21}}$, $B_i = \frac{m_{21}m_{i2} - m_{22}m_{i1}}{m_{21}}$, and $q_i = \frac{-B_i}{A_i} = -\frac{m_{i2}m_{21} - m_{i1}m_{22}}{m_{i1}}$, yields

$$b_i = A_i(\Gamma_2 - q_i)b_2 \tag{2.9}$$

The power absorbed at each power detector can be represented by

$$P_i = |b_i|^2 - |a_i|^2 \tag{2.10}$$

where P_i is the measured power, b_i is the incident wave, a_i is the reflected wave, and $i = 3, 4, 5,$ and 6. Substituting b_i from (2.8), and a_i from (2.2) into (2.10) yields

$$P_i = [1 - \Gamma_i]|A_i|^2|\Gamma_2 - q_i|^2|b_2|^2 \tag{2.11}$$

if one lets $\alpha_i = |A_i|\sqrt{(1 - |\Gamma_i|^2)}$, equation (2.13) becomes

$$P_i = \alpha_i^2|\Gamma_2 - q_i|^2|b_2|^2 \tag{2.12}$$

For equation (2.12), many SPR scholars approached the analysis in two different models to compute solution for Γ_2, i.e. Linear and Quadratic models. This Thesis focuses on the Quadratic model, since its the most used in the literature of SPR relating the reflection coefficient of a DUT to the measured power at the power detectors [1,12,20,23,26,28], and it can be either

$$p_i = \frac{P_i}{P_3} = M_i\frac{|\Gamma_2 - q_i|^2}{|\Gamma_2 - q_3|^2} \tag{2.13}$$

or

$$p_i = \frac{P_i}{P_3} = K_i\frac{|1 + G_i\Gamma_2|^2}{|1 + G_3\Gamma_2|^2} \tag{2.14}$$

where p_i is the normalized power measured with the power measured at port 3, P_3 – commonly used in literature as reference port.

2.2.1 Derivation of $p_i = \frac{P_i}{P_3} = M_i \frac{|\Gamma_2 - q_i|^2}{|\Gamma_2 - q_3|^2}$

This approach is commonly used to derive the quadratic equation relating the power measured at ports 3–6 to the SPR's the measuring plane, port 2. If the SPR is designed with power detector number 3, $D3$, as the reference power measurement port, equation (2.12) can be normalized with power measured at $D3$ and yields

$$p_i = \frac{P_i}{P_3} = \frac{\alpha_i^2 |\Gamma_2 - q_i|^2}{\alpha_3^2 |\Gamma_2 - q_3|^2} = M_i \frac{|\Gamma_2 - q_i|^2}{|\Gamma_2 - q_3|^2} \tag{2.15}$$

where

$$M_i = \frac{|\alpha_i|^2}{|\alpha_3|^2} = \frac{|A_i|^2(1 - |\Gamma_i|^2)}{|A_3|^2(1 - |\Gamma_3|^2)} = \frac{|\frac{m_{i1}}{m_{21}}|^2(1 - |\Gamma_i|^2)}{|\frac{m_{31}}{m_{21}}|^2(1 - |\Gamma_3|^2)} \tag{2.16}$$

for $i = 4, 5$ and 6, and

$$q_i = -\frac{m_{i2}m_{21} - m_{i1}m_{22}}{m_{i1}} = \gamma_i + j\delta_i \tag{2.17}$$

for $i = 3, 4, 5$ and 6.

Equation (2.15) is obtained for a time-stationary, passive and linear six-port junction with no constraints to the power detector input impedance, nor the RF generator's magnitude, phase or internal impedance. Equation (2.15) is a quadratic, circle equation which relates the DUT's reflection coefficient to the incident wave at the power detectors' ports. It is important to realize that from (2.15), 11 real and independent parameters are required to model the six-port reflectometer, hence it is the starting point for the calibration of six-port reflectometers [12].

2.2.2 Derivation $p_i = \frac{P_i}{P_3} = K_i \frac{|1+G_i\Gamma_2|^2}{|1+G_3\Gamma_2|^2}$

Although this derivation is not commonly used in literature, if we let $A_i = \frac{m_{i1}}{m_{21}}$, and $B_i = \frac{m_{i2}m_{21} - m_{i1}m_{22}}{m_{i1}}$, equation (2.8) becomes

$$b_i = A_i(\Gamma_2 + B_i)b_2 \tag{2.18}$$

the power measured at ports 3, 4, 5, and 6 can be determined using

$$P_i = |b_i|^2 - |a_i|^2 \tag{2.19}$$

substituting b_i from (2.23), and a_i from (2.2) into (2.24) yields

$$P_i = |A_i|^2|\Gamma_2 + B_i|^2|b_2|^2 - |\Gamma_i|^2||A_i|^2|\Gamma_2 + B_i|^2|b_2|^2 \tag{2.20}$$

factoring equation (2.23) yields

$$P_i = |A_i|^2|\Gamma_2 + B_i|^2|b_2|^2(1 - |\Gamma_i|^2) \tag{2.21}$$

if we let $|\alpha_i|^2 = |A_i|^2(1 - |\Gamma_i|^2)$, then equation (2.26) becomes

$$P_i = |\alpha_i|^2|\Gamma_2 + B_i|^2|b_2|^2 \quad i = 3...6 \tag{2.22}$$

if we factor $|B_i|^2$ and set $|G_i|^2 = \frac{1}{|B_i|^2}$, then equation (2.27) becomes

$$P_i = |\alpha_i|^2|G_i|^2|1 + G_i\Gamma_2|^2|b_2|^2 \quad i = 3...6 \tag{2.23}$$

letting $K_i = |\alpha_i|^2|G_i|^2$, and normalizing equation (2.28) with P_3, equation (2.28) becomes

$$p_i = \frac{P_i}{P_3} = K_i \frac{|1 + G_i\Gamma_2|^2}{|1 + G_3\Gamma_2|^2} \tag{2.24}$$

where $i = 4, 5$, and 6.

Equation (2.24) describes the relationship between the power ratio measured at ports 3, 4, 5 and 6, and the reflection coefficient at port 2, Γ_2, in terms of three real constants

$$K_i = \frac{|\alpha_i|^2|G_i|^2}{|\alpha_3|^2|G_3|^2} = \frac{\frac{|A_i|^2(1-|\Gamma_i|^2)}{|B_i|^2}}{\frac{|A_3|^2(1-|\Gamma_3|^2)}{|B_3|^2}} = \frac{\frac{|\frac{m_{i1}}{m_{21}}|^2(1-|\Gamma_i|^2)}{|\frac{m_{i2}m_{21}-m_{i1}m_{22}}{m_{i1}}|^2}}{\frac{|\frac{m_{31}}{m_{21}}|^2(1-|\Gamma_3|^2)}{|\frac{m_{32}m_{21}-m_{31}m_{22}}{m_{31}}|^2}} \tag{2.25}$$

where $i = 4, 5$ and 6, and four complex constants,

$$G_i = \frac{1}{B_i} = \frac{m_{i1}}{m_{i2}m_{21} - m_{i1}m_{22}} = \zeta_i + j\sigma_i \tag{2.26}$$

where $i = 3, 4, 5$ and 6.

2.3 Design Criteria & Graphical Interpretation

The graphical interpretation of the equations describing the six-port reflectometer can help understand the relationship between the 11 required parameters (values of q_i, where $i = 3, 4, 5$ and 6, and M_i or G_i, where $i = 4, 5$ and 6), and the design of the six-port reflectometer. Engen and Ghannouchi have discussed the criteria for which an arbitrarily design of six-port reflectometer should satisfy to provide accurate measurements for reflection coefficient of a DUT [13, 14]. This criteria is the values of q_i (where $i = 4, 5$ and 6 providing that reference port is port 3) should be frequency invariant values($|q_i|$ and angles between them are constant) in the reflection coefficient plane, located at the vertices of an equilateral triangle centered at the origin, and outside the unity circle of the reflection coefficient plane. This criteria is important for the accuracy of DUT's reflection coefficient, as if the values of q_i were inside, or on the circumference of the unity circle, will either create ambiguity for the value of the reflection coefficient of a DUT (two or more values for a DUT), or introduce errors to the results.

Using equation (2.15), and knowing that the magnitude of the difference of two complex numbers can be written as

$$|\kappa - \chi|^2 = (\kappa - \chi)(\kappa - \chi)^* = (\kappa - \chi)(\kappa^* - \chi^*) \tag{2.27}$$

$$|\kappa - \chi|^2 = |\kappa|^2 - \kappa^*\chi - \chi^*\kappa + |\chi|^2 \tag{2.28}$$

equation (2.15) can be re-written as

$$\Gamma_{DUT}\Gamma^*_{DUT}(k_i - 1) + \Gamma_{DUT}(q_i^* - k_i q_3^*) + \Gamma^*_{DUT}(q_i - k_i q_3) + (k_i|q_3|^2 - |q_i|^2) = 0 \tag{2.29}$$

where $k_i = \frac{P_i}{P_3 M_i} = \frac{p_i}{M_i}$, and $i = 4, 5$ and 6.

Equation (2.29) can be arranged to be

$$R_i^2 = |\Gamma_{DUT} - C_i|^2 \tag{2.30}$$

and describes three circles in the complex reflection coefficient plane where the centre of the circles is noted by

$$C_i = \frac{k_i q_3 - q_i}{k_i - 1} \tag{2.31}$$

and radii denoted by

$$R_i^2 = \sqrt{|\frac{q_3 - q_i}{k_i - 1}|^2 - \frac{k_i|q_3|^2 - |q_i|^2}{k_i - 1}} \tag{2.32}$$

From equations (2.31) and (2.32) and figure 2.2, we can observe that the centres and the radii of the circles depend on the design of the SPR (i.e. the values of q_i) and the power measured on the measuring ports (i.e. ports 3, 4, 5 and 6). If a DUT is connected to port two of an arbitrary six-port reflectometer, the three circles with centres, C_i, and radii, R_i will

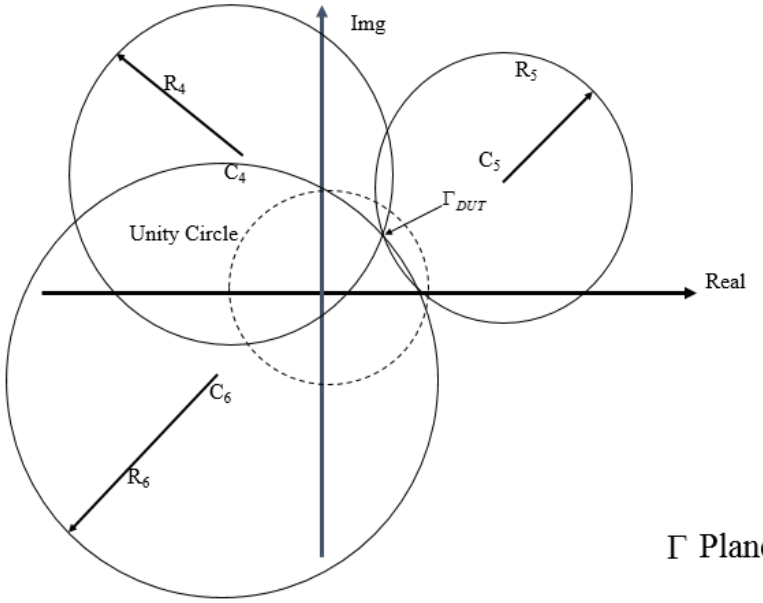

Figure 2.2: A graphical representation of an ideal six-port reflectometer

intersect at a point on the complex reflection coefficient plane, which would represent the complex reflection coefficient of the DUT. However, when the system is realized physically, the solution for the DUT's complex reflection coefficient is in the centre of an intersection region caused by non-ideal behavior of components making the six-port reflectometer, or measurements' and/or calibration's errors. This region is shown in figures 2.3.

The blue shaded region in Figure 2.3 represents the region where the measurement's maximum error is along the walls of the region, and more measurement accuracy is toward the centre of the region. Chapter 3, Calibration Techniques, will discuss various calibration procedures to minimize the imperfection of the circuit and the ways in which other factors impact the accuracy of the measurements. Ambiguity for the value of DUT's reflection coefficient can be introduced if the DUT value equates one of those q_i's; these ambiguities is due to the graphical representation of the six-port reflectometer becomes as five-port reflectometer.

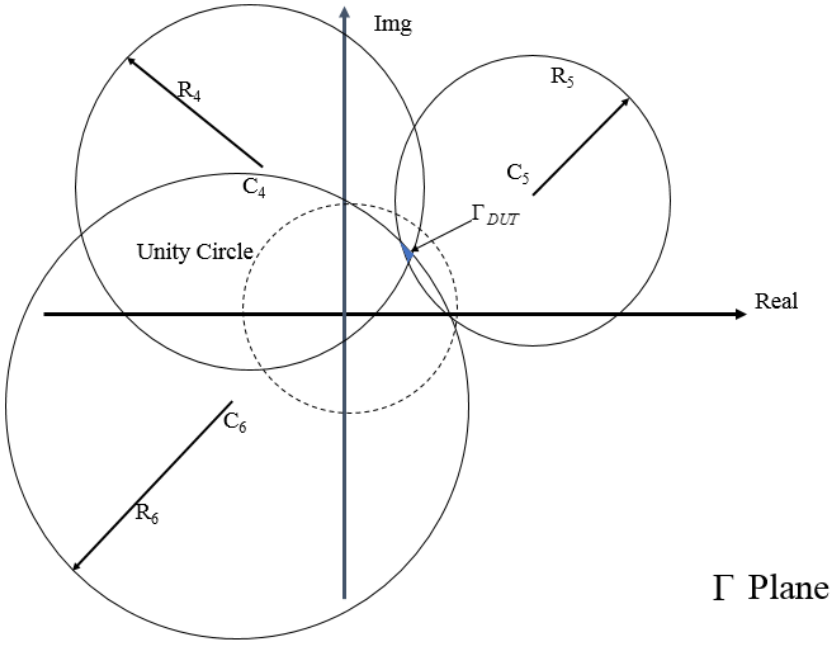

Figure 2.3: A graphical representation of a non-ideal six-port reflectometer

2.3.1 Comparing Six to Four, and Five-port reflectometers

The main advantage of a six-port reflectometer is its ability to provide impedance and complex S-parameter values from scalar power measurements. The use of a four–port reflectometer, which is also capable of providing this ability, however can only measures $|\Gamma_{DUT}|$ and not its phase [14].

If we assume that $P_6 = 0$ (i.e., the six-port reflectometer is actually a five-port reflectometer), then the graphical representation in the complex coefficient plane will be an intersection of two circles at two points, Γ_{DUT} and Γ'_{DUT}.

From Figure 2.4, one can make some observations. There are two values for Γ_{DUT}; provided that the line connecting C_5 and C_4 does not intersect with the unity circle, and assuming a passive DUT, one can be assured that one of those solutions will fall outside the circle's intersection region with the unity circle and may be rejected on this basis ($|\Gamma_{DUT}| \leq 1$). Also, one can note that the angle at the intersected circles is rather small and it is recognizable that the position of Γ_{DUT}, in the direction perpendicular to the line between C_5 and

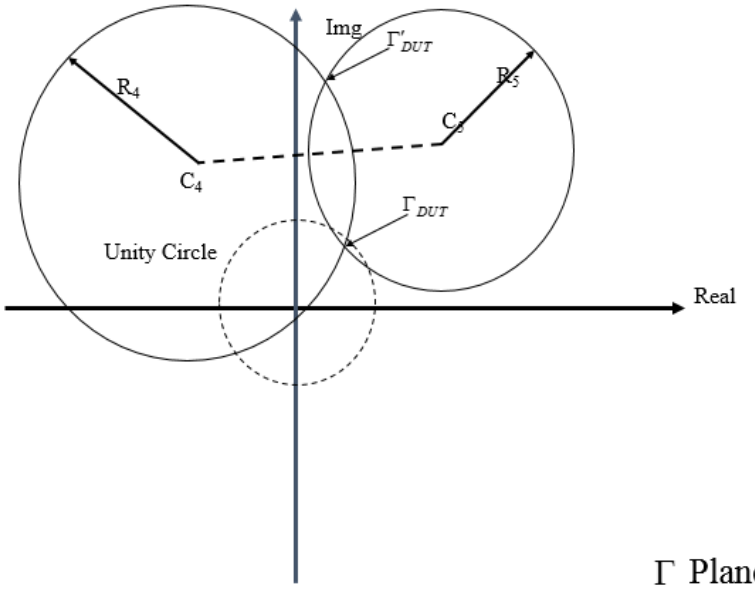

Figure 2.4: A graphical representation of an ideal five-port reflectometer

C_4, has a high sensitivity to errors in the radii R_5 and R_4. In the parallel direction, the sensitivity is appreciably less. Over the range of possible choices of Γ_{DUT} , and especially if Γ_{DUT} moves on the unity circle, one can expect variation in these sensitivities and errors in practical measurements [14].

Adding a sixth port will resolve the ambiguity of pairs of solutions by adding a third circle which will also provide redundancy and substantially increase measurement accuracy. It is important to note that adding additional ports beyond this point, while increasing the redundancy, will not increase the accuracy further, it will only increase the complexity of the measuring system [13].

2.4 Structures and designs of the six-port reflectometer

To design a six-port reflectometer, the most important element that impacts the functionality and the accuracy of measurements is the relative positions of q_i , where $i = 3, 4, 5$ and 6, in the complex plane [14–18]. Various configurations have been proposed for six-

port reflectometer design, all based on an interconnection of several four and/or three port passive junctions such as hybrid couplers and power dividers. In this section, the main designs and structures of six-port reflectometer will be introduced.

2.4.1 Engen's "Preferred" Structure

In 1977, G.F. Engen published a paper for circuit design of six-port reflectometer, and specify one of those three designs as "preferred" six-port circuit [15]. It is important to spend some time analyzing Engen's design because, for decades, his design was adopted by all those who investigated the operation of six-port reflectometers.

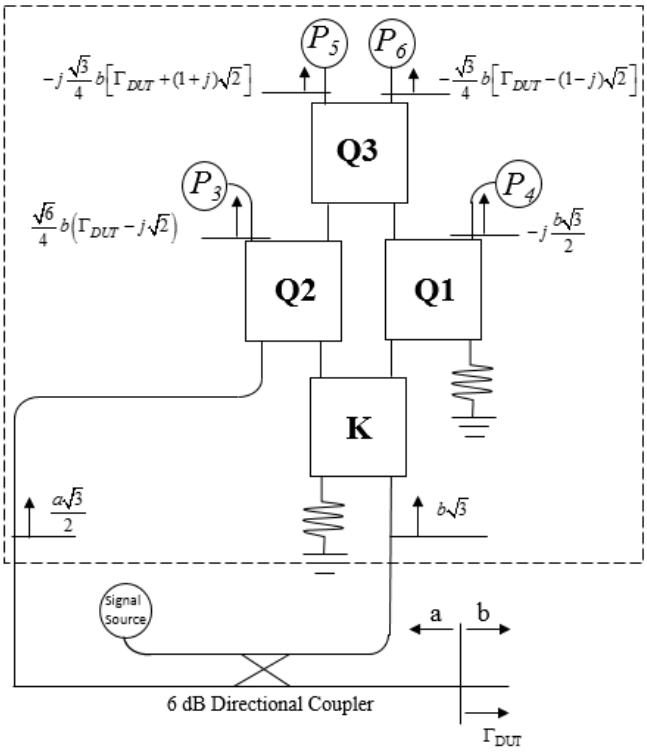

Figure 2.5: Engen's preferred six-port circuit design

The basic configuration of Engen's "preferred" design is shown in Figure 2.5. The normalizing (reference) power port in this design is port number 4, versus port number 3 in equation (2.15). The objective of this design is to have an optimal performance in applying

the six-port technique to the measurements of microwave parameters. Engen's ideal design of a six-port reflectometer is to have $|q_3| = |q_5| = |q_6| = |q|$ (here, we are following Engen's choice for port 4 to be the reference/normalizing power port), and separated in the complex Γ plane by $\pm 120^\circ$ —An equilateral triangle centered at the origin of reflection coefficient plane [14]. However, the design proposed separations from 90° point to $\pm 135^\circ$ with $|q_5| = |q_6| = 2$, and $q_3 = \frac{|q_5|}{\sqrt{2}} = \sqrt{2}$. This design provided the best performance and met the goals at the time. The difference between this design and the "ideal" one was small in comparison to performance degradation, which results from non-ideal components [14]. Thus, the design as shown in Figure 2.5 consisted of three quadrature hybrid couplers and one 180° hybrid coupler. The design was assumed to be lossless (no power disseminated by the terminations at K and Q1 couplers), and one-quarter of the input power will reach the measurement port and be absorbed while the rest will be equally divided among the ports three to six if the load at the DUT's measuring port is a match.

The input levels into the dashed region in Figure 2.5 are $\sqrt{3}b$, and $\frac{a\sqrt{3}}{2}$, where the parameters b and a are of importance in adjusting the magnitude of q and the power levels at the detectors' ports. Let us designate β to be equal to $\sqrt{3}$, and α to be equal to $\frac{\sqrt{3}}{2}$, while the power levels at ports three to six are proportional to β, values of $|q|$ are proportional to $\frac{\beta}{\alpha}$. The significance of β and α is that the ratio between them can limit α to unity and prevent errors and/or ambiguity in measuring the complex reflection coefficient (the system will look as if it is a five-port reflectometer rather than six-port). Acquiring a 6 dB coupler (Figure 2.5) in practice for a specific bandwidth may not be feasible, but 10 dB or 20 dB couplers are readily available in a variety of bandwidths. Therefore, using 10 dB or 20 dB couplers instead of 6 dB coupler will increase β as well as α, and this will not limit α to unity. To resolve this issue, an attenuator can be placed in the line feeding the K coupler to offset the increase in β and impose an upper limit on α, i.e. $\beta = 2\alpha$ [14].

2.4.2 Improved Engen's Structure

Since the introduction of Engen's "preferred" circuit, new technologies have been developed by industry for microwave integrated circuits to meet design specifications such as coupling factors, bandwidth, size and sensitivity to external parameters. Many designs mimic the "preferred" circuit design yet have the advantages of using better technology to achieve the desired bandwidth, size and measurement accuracy. Figure 2.6 shows a frequency compensated optimal six-port reflectometer. This junction, or reflectometer, is Engen's design with three directional hybrid couplers and two power dividers.

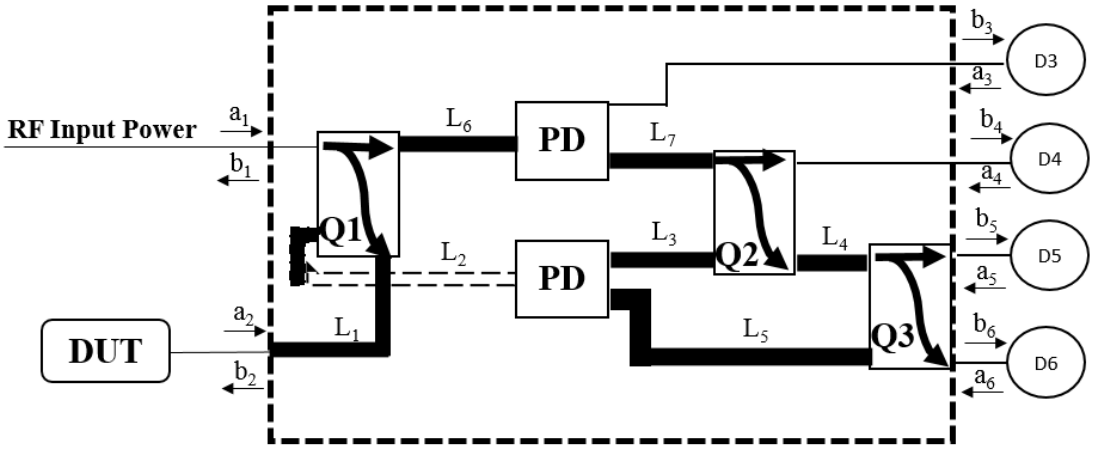

Figure 2.6: Topology of frequency compensated optimal six-port reflectometer

This design will minimize the requirement of the dynamic range of the power detectors and is suitable for a wide frequency band application. The relation between the excitation signal, b_2 , to the input signal, a_1, is:

$$b_2 = ja_1c_1e^{-j(\theta_q+\theta_1)} \tag{2.33}$$

where c_1 and θ_q are the coupling factor and the phase of Q_1, and θ_1 is the electrical length

of L_1. The relation between the reflected signal, a_2, and incident signal, b_2, is:

$$a_2 = \Gamma_{DUT} b_2 \tag{2.34}$$

An algebraic analysis for the wave propagation of an incident signal exciting port 1 and the reflected signal by the DUT with reflection coefficient at port 2 is necessary to determine the expressions for the four signals emerging at the four power detectors [12,21]. Those expressions are:

$$b_3 = \frac{-ib_2 t_1}{c_1\sqrt{2}} e^{-j(\theta_p+\theta_6-\theta_1)} \tag{2.35}$$

$$b_4 = \frac{-ib_2 t_1 c_2}{\sqrt{2}} e^{-j(2\theta_q+\theta_1+\theta_2+\theta_3+\theta_p)} \left(\Gamma - \frac{t_2}{c_1 c_2} e^{-i(-2\theta_1-\theta_2-\theta_3-\theta_q+\theta_6+\theta_7)}\right) \tag{2.36}$$

$$b_5 = \frac{b_2 t_1}{\sqrt{2}} e^{-j(2\theta_q+\theta_1+\theta_2+\theta_5+\theta_p)} \left(t_2 t_3 e^{-i(\theta_3+\theta_4+\theta_q-\theta_5)} + jc_3\right) \left[\Gamma - \frac{-c_2 t_3 e^{-j(-2\theta_1-\theta_2-\theta_5+\theta_4+\theta_6+\theta_7)}}{c_1(t_2 t_3 e^{-j(\theta_3+\theta_4+\theta_q-\theta_5)}) + jc_3}\right] \tag{2.37}$$

$$b_6 = \frac{b_2 t_1}{\sqrt{2}} e^{-j(2\theta_q+\theta_1+\theta_2+\theta_5+\theta_p)} \left(jt_2 c_3 e^{-i(\theta_3+\theta_4+\theta_q-\theta_5)} + t_3\right) \left[\Gamma - \frac{-jc_2 c_3 e^{-j(-2\theta_1-\theta_2-\theta_5+\theta_4+\theta_6+\theta_7)}}{c_1(jt_2 c_3 e^{-j(\theta_3+\theta_4+\theta_q-\theta_5)}) + t_3}\right] \tag{2.38}$$

where θ_q, θ_p, θ_i, c_i, and t_i are the electrical lengths of the lossless directional couplers, the power dividers, transmission lines, the coupling factors, and the transmission factors respectively, and $c_i^2 + t_i^2 = 1$. Note that the expression for b_3 indicates port number 3 as the reference port for this design.

Comparing equations (2.36—2.38) with equation (2.9), i.e. $b_i = A_i(\Gamma_2 - q_i)b_2$, one can

identify that the expressions for the three q_i are:

$$q_4 = \frac{t_2}{c_1 c_2} e^{-j(-2\theta_1-\theta_2-\theta_3+\theta_q+\theta_6+\theta_7)} \tag{2.39}$$

$$q_5 = \frac{-c_2 t_3 e^{-j(-2\theta_1-\theta_2-\theta_5+\theta_4+\theta_6+\theta_7)}}{c_1\left(t_2 t_3 e^{-j(\theta_3+\theta_4+\theta_q-\theta_5)}\right) + jc_3} \tag{2.40}$$

$$q_6 = \frac{-jc_2 c_3 e^{-j(-2\theta_1-\theta_2-\theta_5+\theta_4+\theta_6+\theta_7)}}{c_1\left(jt_2 c_3 e^{-j(\theta_3+\theta_4+\theta_q-\theta_5)}\right) + t_3} \tag{2.41}$$

The frequency compensated optimal term is to compensate for the change of values/positions of q_4, q_5, and q_6 in the reflection coefficient plane as the frequency changes due to the electrical length of the connection lines within the six-port reflectometer. Thus, satisfying the following lines' electrical length equations will compensate for the frequency changes; q_4, q_5, and q_6 values/locations are independent of frequency and will not change in the reflection coefficient plane, which would cause measurements inaccuracy. The electrical lengths of the lines must satisfy the following:

$$2\theta_1 + \theta_2 + \theta_3 + \theta_q = \theta_6 + \theta_7 \tag{2.42}$$

$$\theta_3 + \theta_4 + \theta_q = \theta_5 \tag{2.43}$$

substituting equations (2.42) and (2.43) in (2.36—2.38), we obtain:

$$q_4 = \frac{-c_2}{c_1 c_2} \tag{2.44}$$

$$q_5 = \frac{t_2}{c_1(t_2 + j\frac{t_3}{c_3})} \tag{2.45}$$

$$q_6 = \frac{t_2}{c_1(t_2 - j\frac{t_3}{c_3})} \tag{2.46}$$

Therefore, to obtain an optimal design which satisfies the position of q_i for equations

(2.44–2.46), the coupling factors of the directional couplers must be $c_1 = 0.45$ (6.75 dB), $c_2 = 0.8164$ (1.76 dB) and $c_3 = 0.707$ (3 dB). Designing directional hybrid couplers with those values in practice to operate over a wide range of frequencies is unfeasible and the circuit could be very costly for a small bandwidth.

A frequency compensated quasi-optimal six-port reflectometer is shown in Figure 2.7. This junction uses a variation of Engen's design with a 10 dB coupler, 3 dB attenuator, 3 dB power divider and three 3 dB quadrature hybrid directional couplers. This design was able to overcome the need for directional couplers with various coupling factors. Figure 2.8 shows a frequency compensated quasi-optimal six-port reflectometer realized using miniature hybrid microwave integrated circuits (MHMIC) and a multi-section Wilkinson power divider [13].

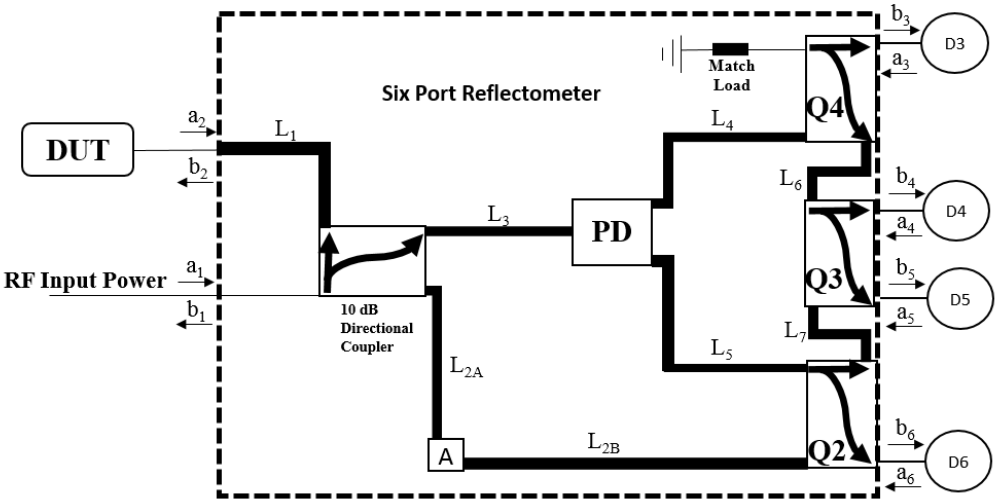

Figure 2.7: Topology for quasi-optimal six-port reflectometer

2.4.3 Other designs

Although newer technology improved microwave circuits, they were still limited by the conductivity of materials used (such as silicon, copper and other compounds) and the frequency bandwidth in which those manufactured components operate optimally.

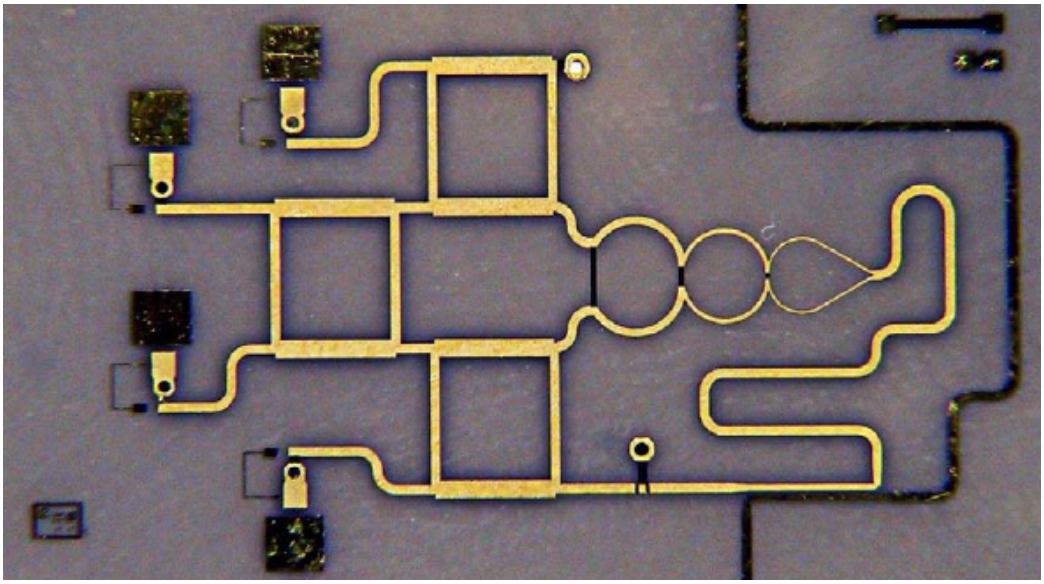

Figure 2.8: quasi-optimal six-port junction [12, p.52]

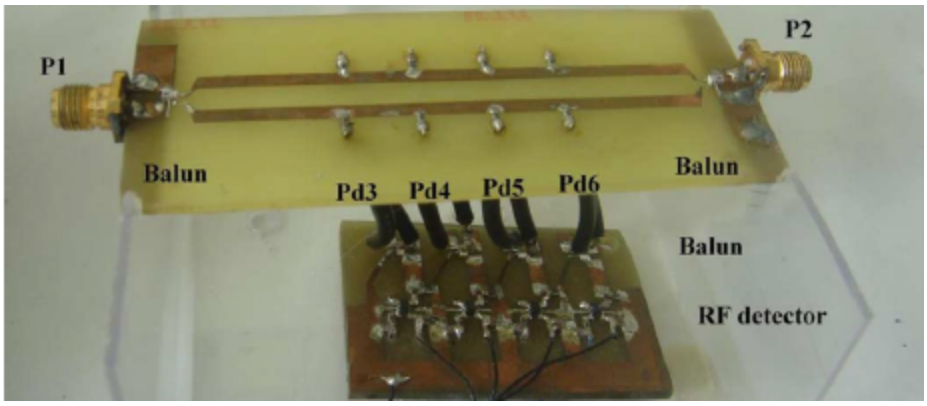

Figure 2.9: Differential six-port reflectometer [19, p.251]

Figure 2.9 shows a new differential six-port reflectometer based on a sampled-line structure which was realized in coplanar strip transmission line form using two baluns to interface with a DUT for complex reflection coefficient measurements. The differential six-port reflectometer is physically small ($10\ cm$ in length, and $5\ cm$ in width) and produced promising results comparable to the ones found with a commercial VNA; however, it was only tested over small bandwidth of approximately 50 MHz [19].

Figure 2.10, a proposed six-port reflectometer using lumped elements, can operate on

a wide range of bandwidth ($0.9 - 5$ GHz) and over a large dynamic range [20]. The design for the positions of $|q|$ and the phase between them was based on Engen's design and provided good results even when the magnitude of the ratio of q_i was greater than 4, and the phases between them were smaller than $25°$ [20]. This simple six-port design was used as a digital modulation homodyne receiver over the entire bandwidth and was physically realized through MMIC technology.

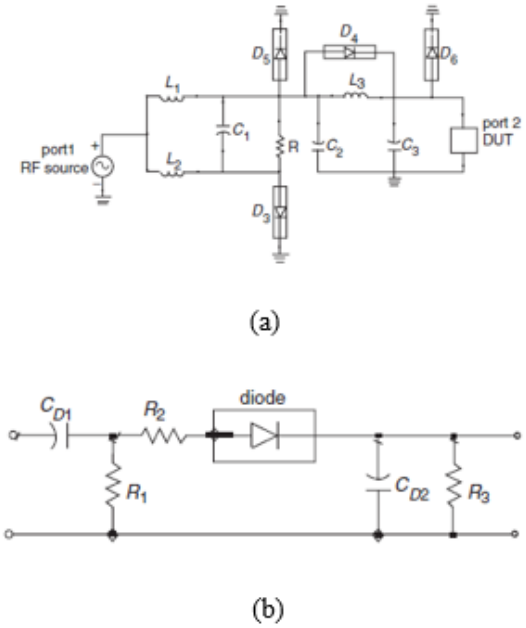

Figure 2.10: a) Wideband six-port Topology, b) Diode detector circuit[20, pg. 302]

2.5 Design Analysis of the Six-port Prototype

The aim of this thesis research is to implement a six-port reflectometer-based VNA operating via independent RF power sources in the RF and microwave frequencies. Therefore, choosing a design that can satisfy the aim as well as the requirements for cost, flexibility, size, and bandwidth, while still providing accurate measurements, is crucial for the success of this thesis. Of all the designs introduced in section 2.5, the six-port reflectometer using lumped elements would meet all these requirements; however, it would have taken a

long time to realize its topology through MMIC technology. Therefore, and as a proof of concept, a frequency compensated quasi-optimal six-port reflectometer using four 3 dB Hybrid 90° couplers and power divider is the most suitable to design, simulate and physically realize using readily available components [34]. Figure 2.11 shows the proposed six-port

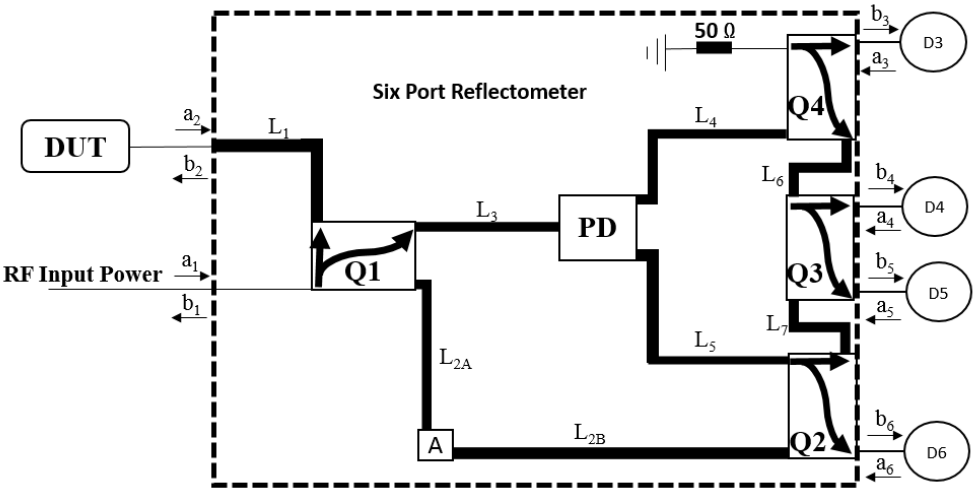

Figure 2.11: Topology of chosen design for six-port reflectometer

reflectometer for this thesis, consisting of four 3 dB Hybrid 90° couplers, power divider, 3 dB attenuater, and connecting lines, L_1–L_7.

Similar to the frequency compensated optimal six-port reflectometer, one can repeat the same algebraic derivation to find the values of $|q_4|$, $|q_5|$, and $|q_6|$ points in the Γ plane with angles $q_4 = \angle\theta^\circ$, $q_5 = \angle(\theta^\circ - 135^\circ)$ and $q_6 = \angle(\theta^\circ + 135^\circ)$, and θ° is an arbitrary reference angle), and applying the value for the 3 dB attenuator ($\sqrt{2}$) to Line L_2, q_i nominal values for $i = 4, 5$ and 6 become:

$$q_4 \approx 2\angle 0^\circ \tag{2.47}$$

$$q_5 \approx 2\angle 270^\circ \tag{2.48}$$

$$q_6 \approx \sqrt{2}\angle 135^\circ \tag{2.49}$$

and the lines' electrical lengths must satisfy:

$$2L_1 + \theta_4 + \theta_q = (L_{2A} + L_{2B}) + L_3 + \theta_p \tag{2.50}$$

$$L_5 + L_7 = L_3 + L_6 \tag{2.51}$$

where L_1–L_7 are the electrical lengths for the lines in Figure 2.11, and θ_p and θ_q are the phase for the power divider and 3 dB Hybrid $90°$ couplers, respectively. Note that this design represents Engen's "Preferred" design, yet with $90°$ shift of of q_i values in the Γ plane.

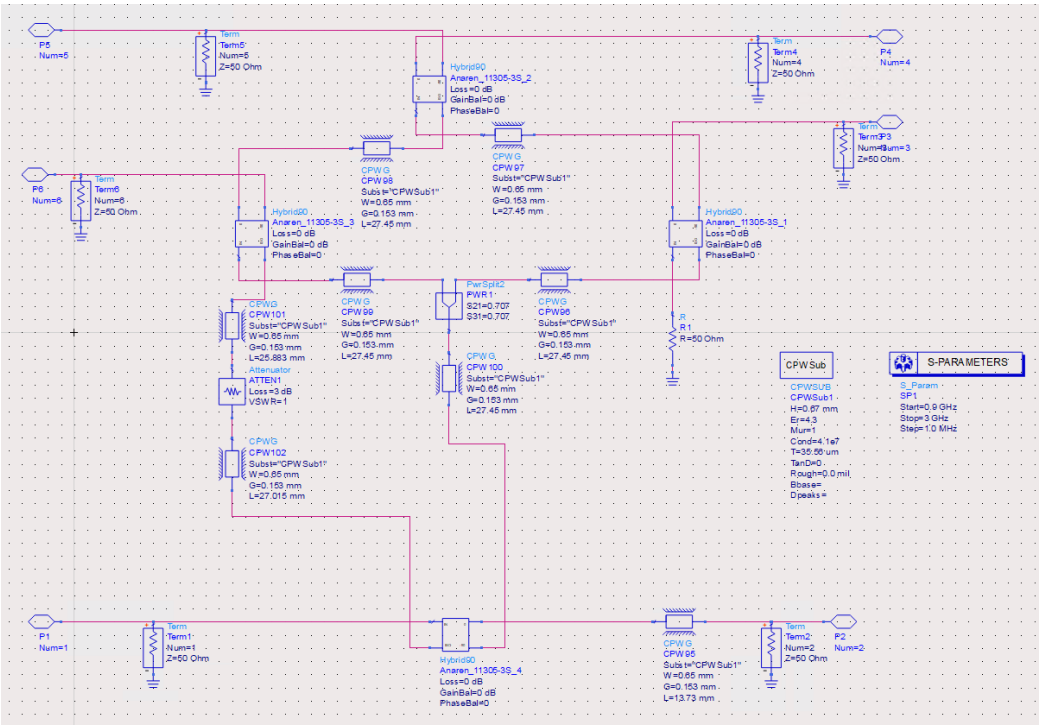

Figure 2.12: ADS schematics for six-port reflectometer's prototype

To simulate the circuit in Figure 2.11, Advanced Design System (ADS) version 19 (update 1),from Keysight Technologies was used. Co-planar with ground (CPW) substrate of $\epsilon_r = 4.3$ (FR4), thickness of 0.67 mm was used to setup the substrate for the simulation. Ports 1–6 were matching the impedance of the circuit, i.e. 50Ω. The circuit was designed using four ideal 3 dB Hybrid 90° couplers, ideal Wilkinson's power divider, and the connecting lines were designed to be 50Ω and satisfying the electrical length in equations (2.50) and (2.51).

Analysis of the circuit in Figure 2.11 is required to determined the values for q_i in terms of S-parameters. From figure 2.11, since all ports in Figure 2.12 were matched (i.e. 50Ω), the reflection coefficient of the power detectors' ports, Γ_i ($i = 3, 4, 5,$ and 6), is zero. This leads equation (2.3) to be

$$\begin{bmatrix} b_1 \\ b_2 \\ 0 \\ 0 \\ 0 \\ 0 \end{bmatrix} = \begin{bmatrix} S_{11} & S_{12} & 0 & 0 & 0 & 0 \\ S_{21} & S_{22} & 0 & 0 & 0 & 0 \\ S_{31} & S_{32} & -1 & 0 & 0 & 0 \\ S_{41} & S_{42} & 0 & -1 & 0 & 0 \\ S_{51} & S_{52} & 0 & 0 & -1 & 0 \\ S_{61} & S_{62} & 0 & 0 & 0 & -1 \end{bmatrix} \begin{bmatrix} a_1 \\ a_2 \\ b_3 \\ b_4 \\ b_5 \\ b_6 \end{bmatrix} \tag{2.52}$$

and the solution for b_1, b_2, and b_i are

$$b_1 = S_{11}a_1 + S_{12}a_2 \tag{2.53}$$

$$b_2 = S_{21}a_1 + S_{22}a_2 \tag{2.54}$$

$$b_i = S_{i1}a_1 + S_{i2}a_2 \tag{2.55}$$

Substitution of $b_2 = \frac{a_2}{\Gamma_{DUT}}$ in equation (2.54) and solving for a_1, yields that

$$a_1 = \big(\frac{1}{\Gamma_{DUT}} - S_{22}\big)\frac{a_2}{S_{21}} \tag{2.56}$$

Substituting of a_1 (equation (2.56)) and $a_2 = \Gamma_{DUT} b_2$ into equation (2.55), b_i becomes

$$b_i = \frac{S_{i1}}{S_{21}}\big(1 - \big(\frac{S_{22}S_{i1} - S_{21}S_{i2}}{S_{i1}}\Gamma_{DUT}\big)\big)b_2 \tag{2.57}$$

letting

$$A_i = \frac{S_{i1}}{S_{21}} \tag{2.58}$$

$$B_i = \frac{S_{21}S_{i2} - S_{22}S_{i1}}{S_{21}} \tag{2.59}$$

$$q_i = \frac{-A_i}{B_i} = \frac{S_{i1}}{S_{22}S_{i1} - S_{i2}S_{21}} \tag{2.60}$$

and substituting the values of A_i and q_i into equation (2.59) yields

$$b_i = A_i(1 - \big(\frac{\Gamma_{DUT}}{q_i}\big))b_2 = A_i\big(\frac{q_i - \Gamma_{DUT}}{q_i}\big)b_2 \tag{2.61}$$

Factoring $\frac{-1}{q_i}$ from equation (2.63) yields

$$b_i = \frac{-A_i}{q_i}\big(\Gamma_{DUT} - q_i\big)b_2 = B_i\big(\Gamma_{DUT} - q_i\big)b_2 \tag{2.62}$$

where $i = 3, 4, 5$ and 6. Since all power measuring ports are matched ($\Gamma_i = 0$, where $i = 3, 4, 5$ and 6), the power absorbed at each power detector can be written as

$$P_i = |b_i|^2 = |B_i|^2|\Gamma_{DUT} - q_i|^2|b_2|^2 \tag{2.63}$$

where B_i and q_i are known, i.e. equations (2.59) and (2.60) respectively. Normalizing the power measured in equation (2.63) with the reference power measured, P_3, equation (2.63)

becomes

$$p_i = \frac{P_i}{P_3} = \frac{|B_i|^2|\Gamma_{DUT} - q_i|^2}{|B_3|^2|\Gamma_{DUT} - q_3|^2} = M_i \frac{|\Gamma_{DUT} - q_i|^2}{|\Gamma_{DUT} - q_3|^2} \tag{2.64}$$

where $M_i = \frac{|B_i|^2}{|B_3|^2}$, and $i = 4, 5,$ and 6.

Similar to the derivation in section 2.2.1, Equation (2.64) describes the relationship between the power ratio measured at ports 3, 4, 5 and 6, and the reflection coefficient at port 2, Γ_{DUT}, in terms of three real constants

$$M_i = \frac{|B_i|^2}{|B_3|^2} = \frac{|S_{21}S_{i2} - S_{22}S_{i1}|^2}{|S_{21}S_{32} - S_{22}S_{31}|^2} \tag{2.65}$$

where $i = 4, 5$ and 6, and four complex constants,

$$q_i = \frac{-A_i}{B_i} = \frac{S_{i1}}{S_{22}S_{i1} - S_{i2}S_{21}} = \gamma_i + j\delta_i \tag{2.66}$$

where $i = 3, 4, 5$ and 6.

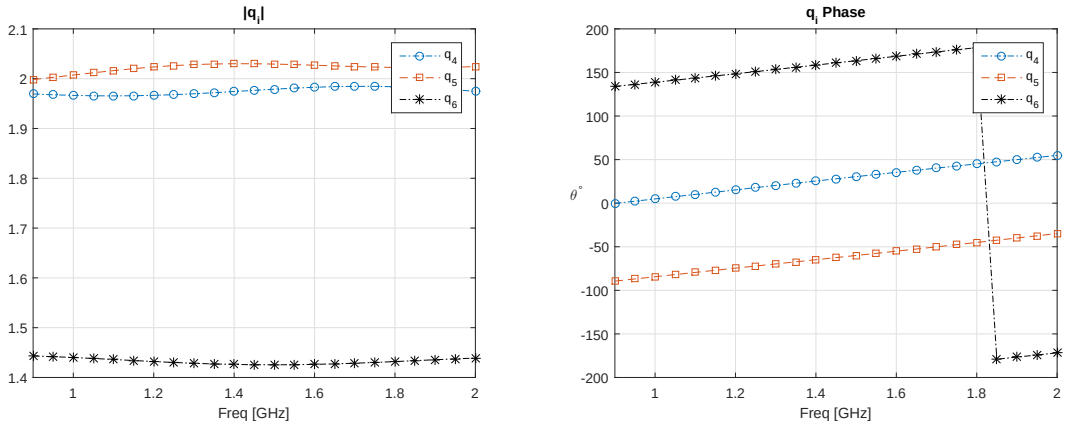

(a) q_i Magnitude (b) q_i Phase

Figure 2.13: q_i simulated results for Ideal Six-port Reflectometer

Figure 2.13 demonstrate an agreement between ADS simulation and our expected values for q_i's analysis (equations (2.47–2.49)).

To realize the prototype physically, MIC components were identified. Table 2.1 pro-

vides a list of MIC components which potentially meet the requirements to physically realize the six-port reflectometer. These components' electrical parameters were used in the simulation of the six-port reflectometer prototype. The simulation accounted for all the losses and limitations of those MIC components and the nominal simulation temperature was set to default, which is $25^{\circ}\,C$.

Table 2.1: Main MIC components' parameters used in the Six-port Reflectometer simulation

3dB–90° Hybrid Coupler: Anaren model 11035-3S					
Freq [GHz]	Isolation [dB]	Insertion Loss [dB]	Phase Balance [degrees]	Amp Balance [dB]	SWVR
1.0-2.0	20	0.45	± 3	± 0.55	1.3:1
Wilkinson's Power Divider:Anaren model PD0922J5050S2HF					
Freq [GHz]	Isolation [dB]	Insertion Loss [dB]	Phase Balance [degrees]	Amp Balance [dB]	In/Out [W]
0.95-2.15	12	0.7-0.8	1.0-3.0	0.1-0.5	50/50

In addition to the modifications of the connecting lines, other connecting lines such as RF input power line and power detector connecting lines were designed at 50Ω impedance and integrated with the prototype circuit. The power detectors connecting lines were designed with an electrical length of 180° to enable better management of components in the PCB and to maintain a small and compact circuit. modifications to the substrate and dimensions of the lines were also made to facilitate future manufacturing of the prototype.

Figure 2.14 shows the simulated circuit with MIC component parameters utilized, as well as the other aforementioned connecting lines. Figure 2.15 shows the simulated q_i for the prototype using the MIC components. The difference in the magnitude of q_4 and q_5, as well as the phase of q_6 from the ideal circuit, does not impact the performance of the circuit, as this will be shown in the next chapter.

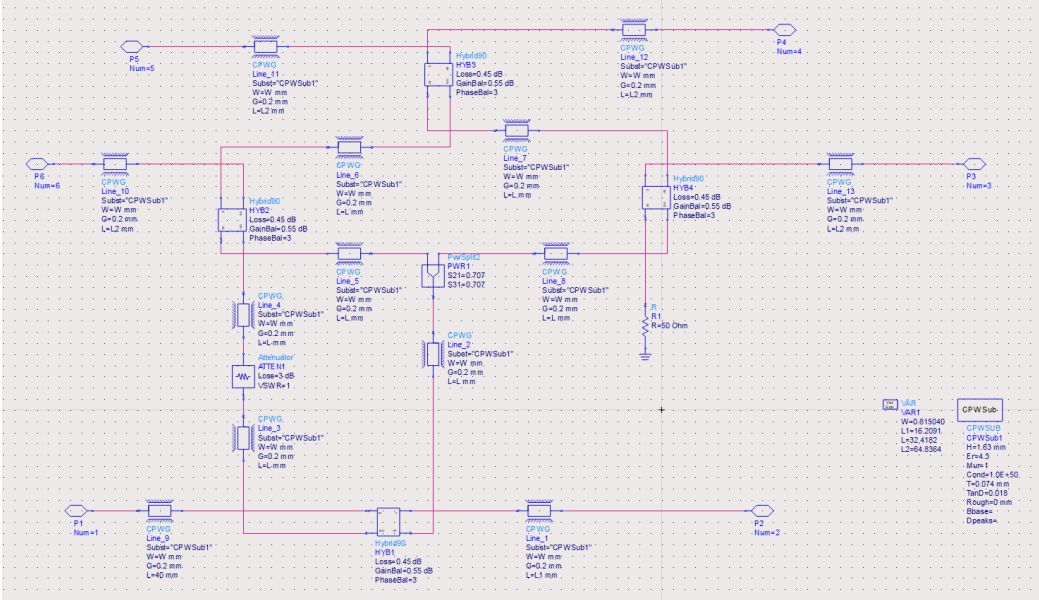

Figure 2.14: ADS six-port reflectometer with MIC component parameters

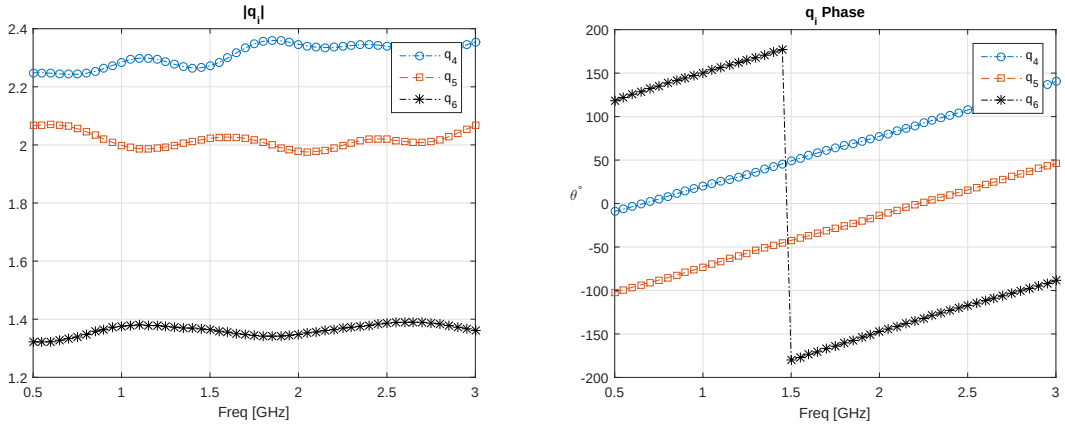

(a) q_i Magnitude (b) q_i Phase

Figure 2.15: q_i simulated results for SPR prototype using MIC parameters and modified lines

Chapter 3

Calibration Techniques

In chapter two, theory and designs of six-port reflectometers were presented. It was shown that 11 parameters are required to compute the reflection coefficient of a DUT. Many methods and procedures for calibration (determination of the required 11 parameters) have been presented since the inception of the six-port reflectometer; these range from using sliding termination, to seven, five or three calibration standards, to an adoption of the diode power detector linearization technique called dual toning or "self-calibrated" based on active load synthesis techniques [13, 22, 24, 25]. The number of known calibration standards and the level of computation are the most important aspects in selecting the calibration technique. There are two categories of calibration techniques; linear and nonlinear [13, 24]. It is important to note here that all power detectors are permanently connected to the SPR being calibrated. In this chapter, the focus is on the nonlinear technique, as it aligns with chosen quadratic model design of the prototype, and specific discussion of the Six-to-Four ports reduction, and the Explicit calibration techniques is presented. Although both techniques utilize number of calibration standards, a novel approach to the Explicit calibration technique proved validity. Simulated results for number of synthesized DUTs using the chosen design are also presented in this chapter.

3.1 Six-to-Four Port Reduction Technique

This technique is the most common to calibrate a six-port reflectometer. The technique is based on a bi-linear transformation of the six-port reflectometer to an easily calibrated

system of an ideal reflectometer and two-port network called an error box; see figure 3.1. There are other techniques to calibrate a six-port reflectometer, however, this technique has the advantage of not having to calculate the 11 independent parameters simultaneously; rather, nine unknown standards can be used to calibrate the ideal reflectometer, then three additional known standards are used for calibrating the error box parameters. The procedure is described thoroughly in Engen [24], Hodgett et al [25], and Ghanoochi [13]. There is also a newer reduction algorithm described in Potter et al [30]. Therefore, this section will present this method briefly, leaving detailed research to the reader's preferences.

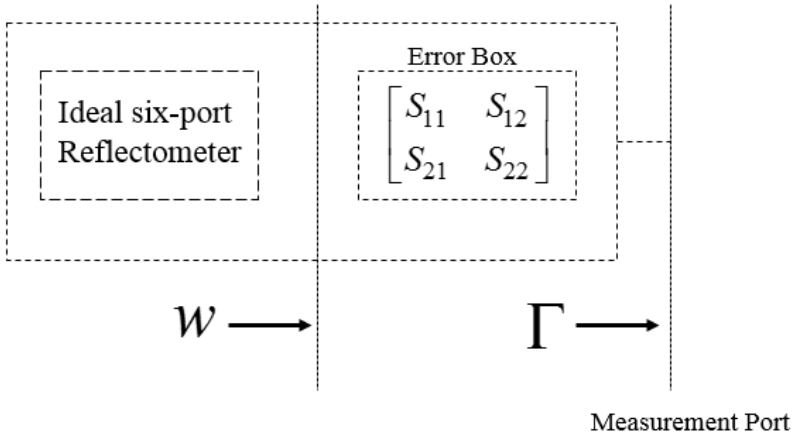

Figure 3.1: Six-to-four- port reflectometer representation

Equation (2.15) can be re-written as

$$P_i = |w_i|^2 = \left| \frac{d_i \Gamma - e_i}{c_3 \Gamma + 1} \right|^2 \tag{3.1}$$

where $d_i = \frac{-M_i}{q_3} = S_{12}^{EB} S_{21}^{EB} - S_{11}^{EB} S_{22}^{EB}$, $e_i = \frac{q_i M_i}{q_3} = S_{11}^{EB}$, and $c_3 = \frac{1}{q_3} = -S_{22}^{EB}$, and $i = 4, 5$ and 6. The superscription of EB denotes the S-parameters for the error Box. Solving equation (3.1) for Γ yields,

$$\Gamma = \frac{e_i - w_i}{c_3 w_i - d_i} \tag{3.2}$$

To determine the value for *w*, one requires minimum of nine known standards (matched, open and short can be used). Taking power measurements from the four diode power detectors for those nine standards will produce a 4×9 matrix. This matrix can be normalized with the reference port power measurement (port 3) to produce a 3×9 matrix, which can be used to solve for $x_1...x_9$ in the following

$$x_1Q_4^2 + x_2Q_5^2 + x_3Q_6^2 + x_4Q_5Q_6 + x_5Q_4Q_6 + x_6Q_5Q_6 + x_7Q_4 + x_8Q_5 + x_9Q_6 = -1 \quad (3.3)$$

where Q_4, Q_5 and Q_6 are the normalized power measurements for port 4, 5 and 6. Once the values for $x_1...x_9$ are determined, they will be used to calculate the following parameters:

$$r = \frac{2x_5 - x_7x_9}{2x_1x_9 - x_5x_7} \quad (3.4)$$

$$q = \frac{2x_4 - x_7x_8}{2x_1x_8 - x_4x_7} \quad (3.5)$$

$$p = r + q + \left(\frac{x_7}{x_1}\right) \quad (3.6)$$

$$A^2 = \sqrt{prx_2} \quad (3.7)$$

$$B^2 = \sqrt{pqx_3} \quad (3.8)$$

Parameters r, p, q, A^2 and B^2 are an approximation for the five parameters required to determine w, the reflection coefficient of the ideal six-port reflectometer (Figure 3.1). In fact, Engen remarks that they represent conditions of tangency of three planes to the ellipsoidal paraboloid represented in the following equation

$$\begin{aligned} pQ_4^2 + gA_5^2Q_5^2 + rA_6^2Q_6^2 + (r-p-g)A_5^2Q_5Q_6 + \\ (g-p-r)A_6^2Q_4Q_6 + (p-g-r)A_5^2A_6^2Q_5Q_6 + p(p-g-r)Q_4 + \\ g(g-p-r)A_5^2Q_5 + r(r-p-g)A_6^2Q_6 + pgr = -1 \end{aligned} \quad (3.9)$$

which is quadric in w plane [22].

The solution of those five parameters can be refined by using a standard optimization technique, such as Gauss-Newton, or Margetts-Lambert. Once those five parameters are optimized, w can be calculated using [24]:

$$w = \frac{Q_4 - A^2 Q_2}{2\sqrt{r}} \pm j \frac{\left[r(p+q-r) + (p-q+r)Q_4 - (p-q-r)A^2 Q_2 - 2rB^2 Q_3 \right]}{2\sqrt{r(2pq + 2qr_p r - p^2 - q^2 - r^2)}} \tag{3.10}$$

The sign ambiguity can be resolved using a known standard. Once w is determined, three known standards (e.g. matched, open and short circuits) can be used to find the error box parameters using the following linear system

$$w_i^S \Gamma_i^S c - \Gamma_i^S d - e = w_i^S \tag{3.11}$$

the superscript, S, indicates the standard used, and $i = 1, 2$ and 3.

Although nine standards are required to determine w, this technique requires 13 standards in practice [34]. These 13 standards are designed to be distributed symmetrically across the Smith chart to ensure distribution over the entire six-port reflectometer's operational bandwidth. See Figure 3.2 where the 13 standards are noted with ★.

This technique is quite complicated and increases the potential for error when many standards are being replaced one after another. The five parameters required to calculate w will provide approximated values; to refine them, computational effort and an initial value/guess must be determined and incorporated in the computation. Finally, w calculation depends on an accurate power measurements from those four diode power detectors, hence a robust diode linearization procedure must be in situ. All these reasons make the next calibration technique more desirable as, ideally, if one can determine the S-parameters of the six-port reflectometer, the only standards required are those for confirmation of computed

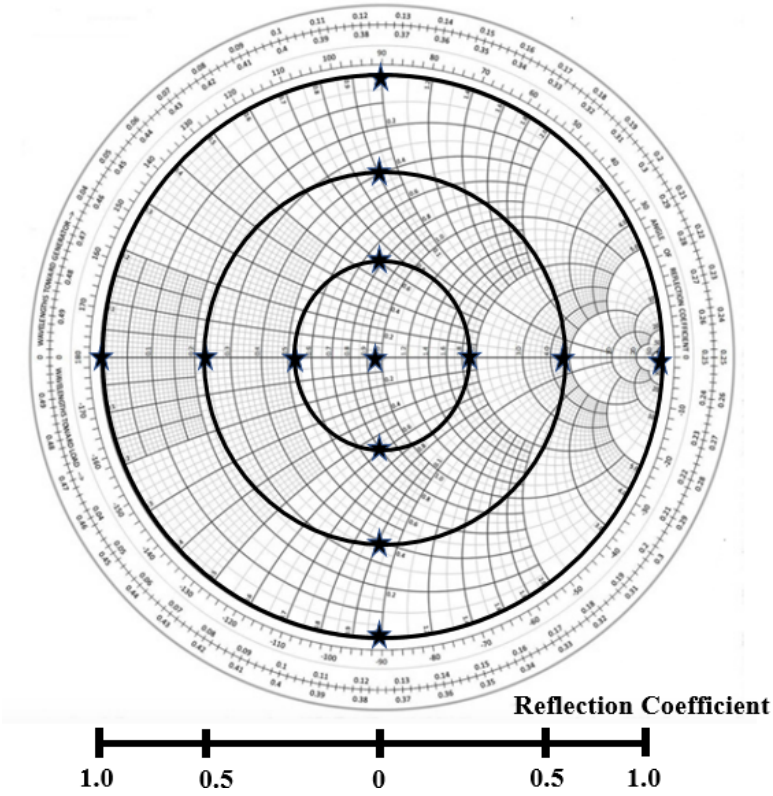

Figure 3.2: 13 standard's distribution on Smith chart

reflection coefficient of a standard, i.e. DUT.

3.2 An Explicit Calibration Technique

We discussed in chapter two the chosen design and the derivation of the following equation

$$p_i = \frac{P_i}{P_3} = \frac{|B_i|^2|\Gamma_{DUT} - q_i|^2}{|B_3|^2|\Gamma_{DUT} - q_3|^2} = M_i \frac{|\Gamma_{DUT} - q_i|^2}{|\Gamma_{DUT} - q_3|^2} \tag{3.12}$$

where $i = 4, 5$, and 6,

$$M_i = \frac{|B_i|^2}{|B_3|^2} = \frac{|S_{21}S_{i2} - S_{22}S_{i1}|^2}{|S_{21}S_{32} - S_{22}S_{31}|^2} \tag{3.13}$$

where $i = 4, 5$ and 6 for 3 scalar constants, and

$$q_i = \frac{-A_i}{B_i} = \frac{S_{i1}}{S_{22}S_{i1} - S_{i2}S_{21}} = \gamma_i + j\delta_i \tag{3.14}$$

where $i = 3, 4, 5$ and 6 for four complex constants. Equation 2.13 assumes that $\Gamma_i = 0$ for $i = 3, 4, 5$ and 6, and relates the measured power at ports 3, 4, 5 and 6 to the reflection coefficient of a DUT placed on the measuring plane, port 2.

Developed by Hoer [27], and confirmed by Wood [28], the reflection coefficient of a DUT, using an arbitrary six-port reflectometer, can be determined by

$$\Gamma_{DUT} = \frac{\sum_{i=3}^{6}(F_i + jE_i)\frac{P_i}{P_3}}{1 + \sum_{i=4}^{6} H_i \frac{P_i}{P_3}} \tag{3.15}$$

where F_i, E_i and H_i are the 11 parameters required to calibrate an arbitrary six-port reflectometer. Xiong, Wood, Li and Bosisio, and Somlo and Hunter have described in detail how to obtain these parameters using power measurements of synthesized active loads, or five, or four open/short calibration standards [22, 28, 29, 30, 31]. The calibration parameters (F_i, E_i and H_i) can be computed using the following explicit equations

$$k = \gamma_4(\delta_5 - \delta_6) + \gamma_5(\delta_6 - \delta_4) + \gamma_6(\delta_4 - \delta_5) \tag{3.16}$$

$$F_3 = \frac{-1}{2k}\left[|q_4|^2(\delta_5 - \delta_6) + |q_5|^2(\delta_6 - \delta_4) + |q_6|^2(\delta_4 - \delta_5)\right] \tag{3.17}$$

$$F_4 = \frac{1}{2kM_4}\left[|q_3|^2(\delta_5 - \delta_6) + |q_5|^2(\delta_6 - \delta_3) + |q_6|^2(\delta_3 - \delta_5)\right] \tag{3.18}$$

$$F_5 = \frac{-1}{2kM_5}\left[|q_3|^2(\delta_4 - \delta_6) + |q_4|^2(\delta_6 - \delta_3) + |q_6|^2(\delta_3 - \delta_4)\right] \tag{3.19}$$

$$F_6 = \frac{1}{2kM_6}\left[|q_3|^2(\delta_4 - \delta_5) + |q_4|^2(\delta_5 - \delta_3) + |q_5|^2(\delta_3 - \delta_4)\right] \tag{3.20}$$

$$E_3 = \frac{1}{2k}\left[|q_4|^2(\gamma_5-\gamma_6)+|q_5|^2(\gamma_6-\gamma_4)+|q_6|^2(\gamma_4-\gamma_5)\right] \tag{3.21}$$

$$E_4 = \frac{-1}{2kM_4}\left[|q_3|^2(\gamma_5-\gamma_6)+|q_5|^2(\gamma_6-\gamma_3)+|q_6|^2(\gamma_3-\gamma_5)\right] \tag{3.22}$$

$$E_5 = \frac{1}{2kM_5}\left[|q_3|^2(\gamma_4-\gamma_6)+|q_4|^2(\gamma_6-\gamma_3)+|q_6|^2(\gamma_3-\gamma_4)\right] \tag{3.23}$$

$$E_6 = \frac{-1}{2kM_6}\left[|q_3|^2(\gamma_4-\gamma_5)+|q_4|^2(\gamma_5-\gamma_3)+|q_5|^2(\gamma_3-\gamma_4)\right] \tag{3.24}$$

$$H_4 = \frac{1}{kM_4}\left[\gamma_3(\delta_5-\delta_6)+\gamma_5(\delta_6-\delta_3)+\gamma_6(\delta_3-\delta_5)\right] \tag{3.25}$$

$$H_5 = \frac{-1}{kM_5}\left[\gamma_3(\delta_4-\delta_6)+\gamma_4(\delta_6-\delta_3)+\gamma_6(\delta_3-\delta_4)\right] \tag{3.26}$$

$$H_6 = \frac{1}{kM_6}\left[\gamma_3(\delta_4-\delta_5)+\gamma_4(\delta_5-\delta_3)+\gamma_5(\delta_3-\delta_4)\right] \tag{3.27}$$

where M_i, δ_i, and γ_i (for $i = 3, 4, 5,$ and 6) values are from equations (3.13) and (3.14). However, using a VNA to measure the S-parameters of the six-port reflectometer can permit the computation of M_i and q_i values required to compute these explicit equations for the calibration parameters, without the need for power measurements of any calibration standards. This approach is novel in comparison to the standard Explicit calibration technique which was developed utilizing number of calibration standards.

3.3 Six-port Reflectometer Simulation Results

To validate the novel approach to the Explicit calibration technique, S-parameters for the six-port reflectometer in Figure 2.14 were measured using ADS simulator for frequency range of 0.5–3 GHz, and three different DUTs were created in ADS to provide different complex reflection coefficients over the range of the simulated frequencies. Once the six-port reflectometer's S-parameters and the three DUTs' true reflection coefficients were recorded, computations for calibration factors (F_i, E_i and H_i) were conducted and values were stored, then the DUTs were placed for power measurement simulation using power probes within ADS. See Figures 3.3 for the setup in ADS.

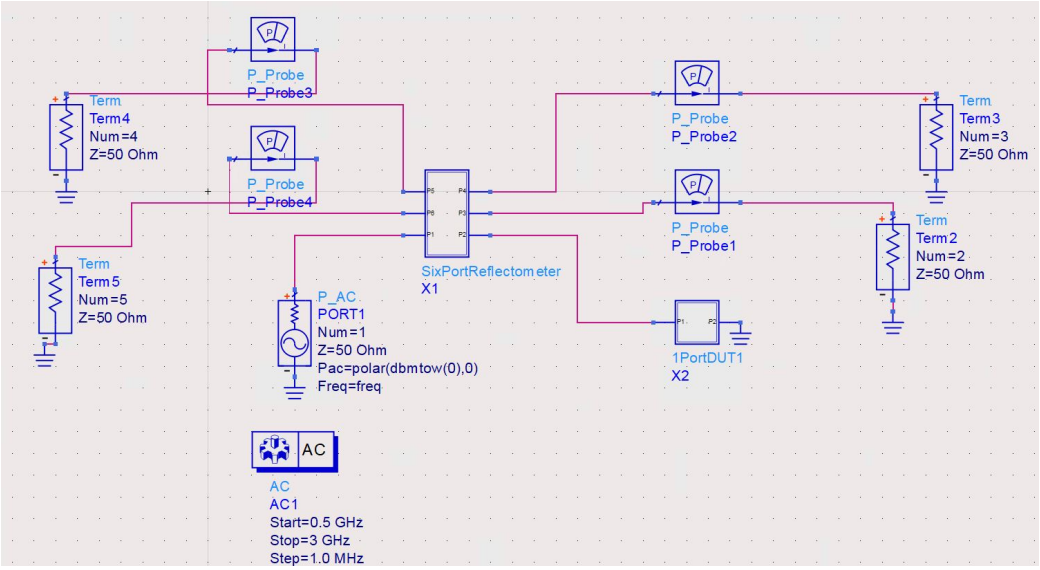

Figure 3.3: Six-port reflectometer presentation in ADS

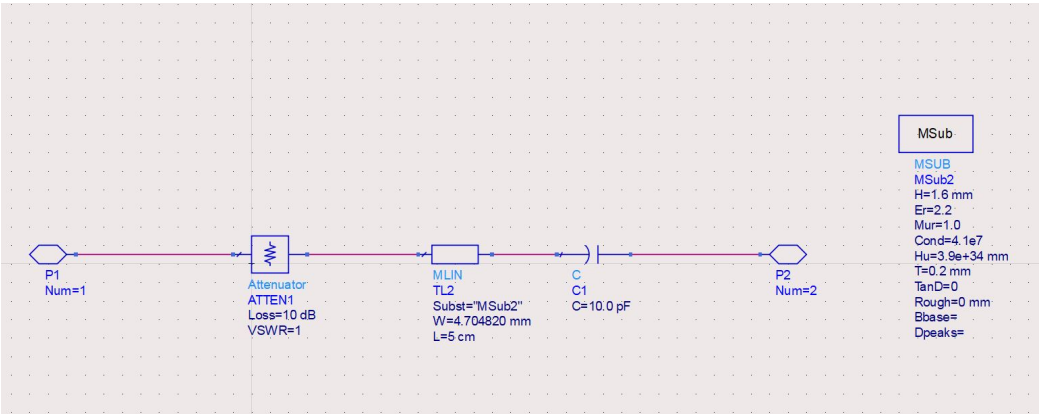

Figure 3.4: 1st DUT design

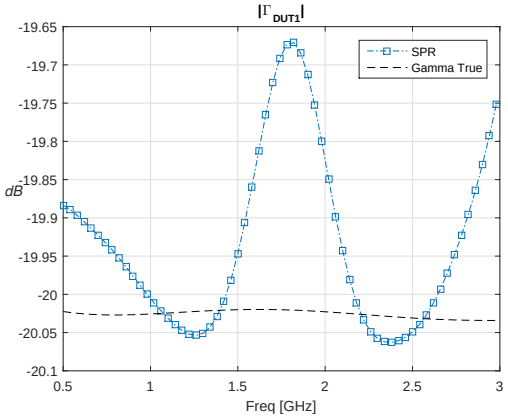

(a) 1st DUT magnitude

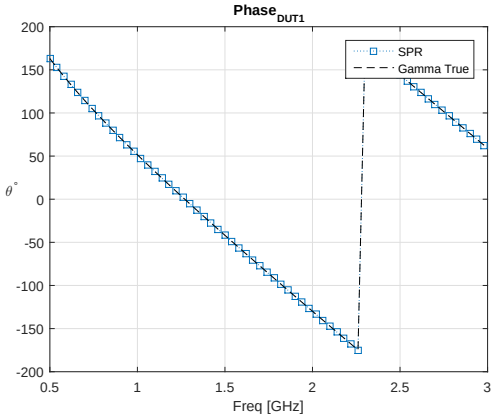

(b) 1st DUT phase

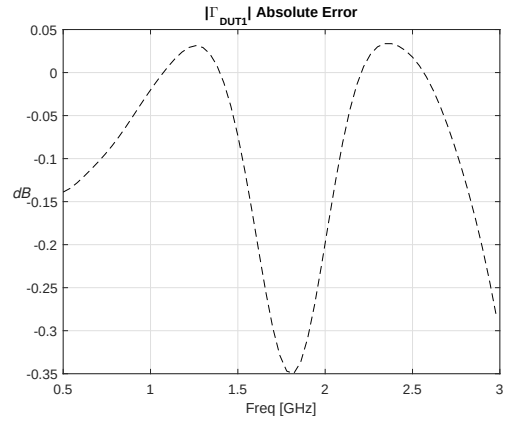

(c) magnitude absolute error

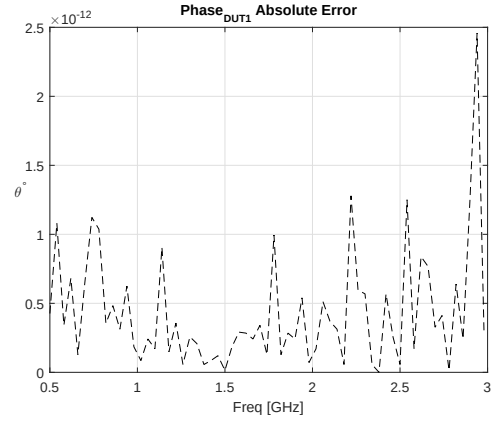

(d) phase error

Figure 3.5: 1st DUT simulation results

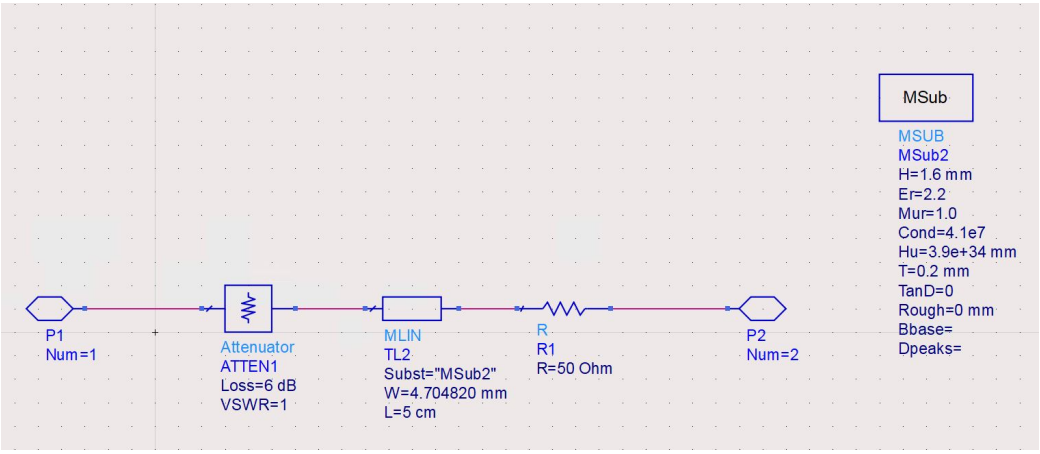

Figure 3.6: 2nd DUT design

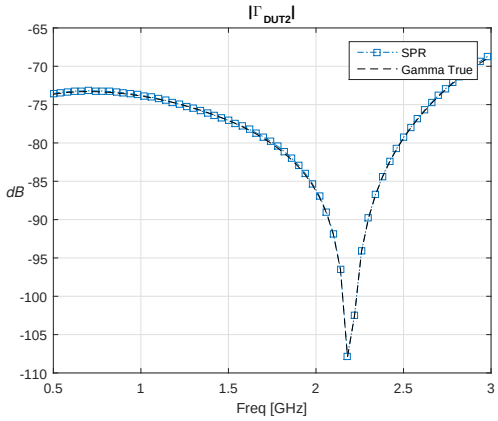

(a) 2nd DUT magnitude

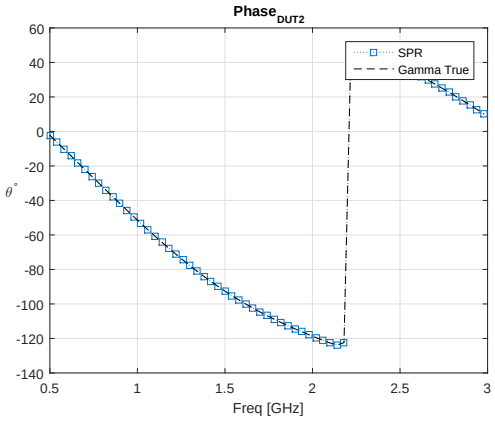

(b) 2nd DUT phase

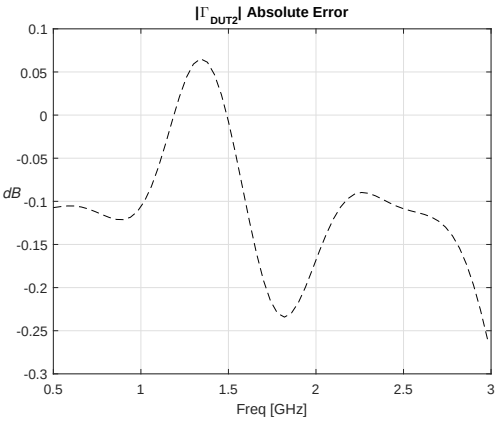

(c) magnitude absolute error

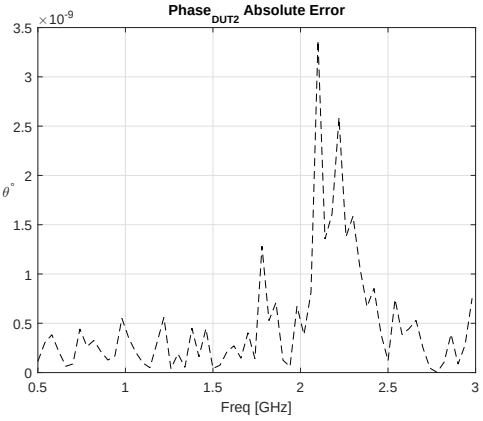

(d) phase error

Figure 3.7: 2nd DUT simulation results

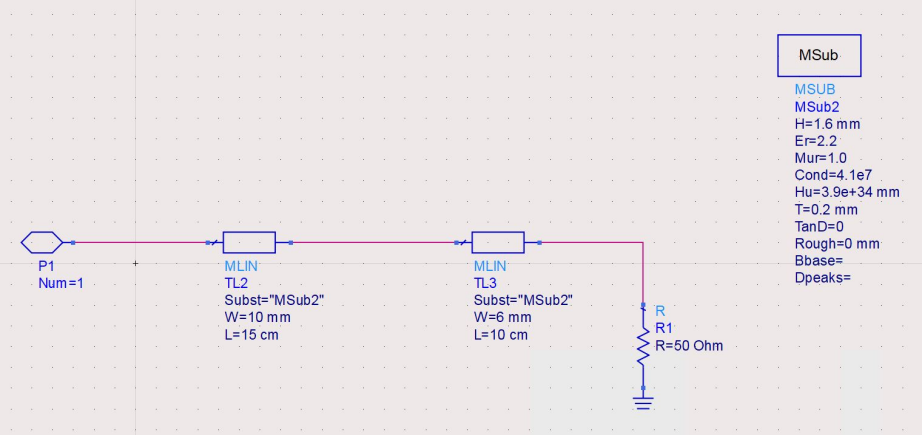

Figure 3.8: 3rd DUT design

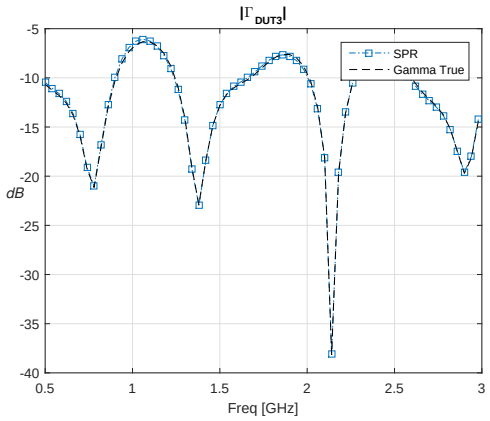

(a) 3rd DUT magnitude

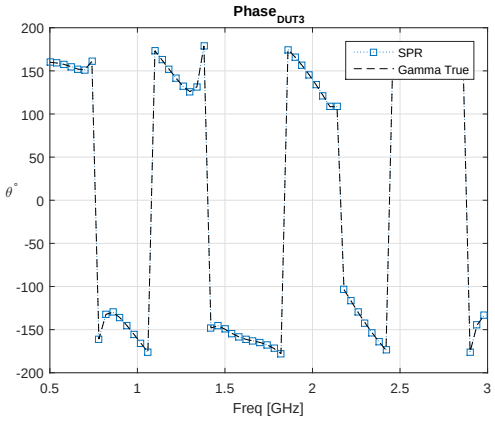

(b) 3rd DUT phase

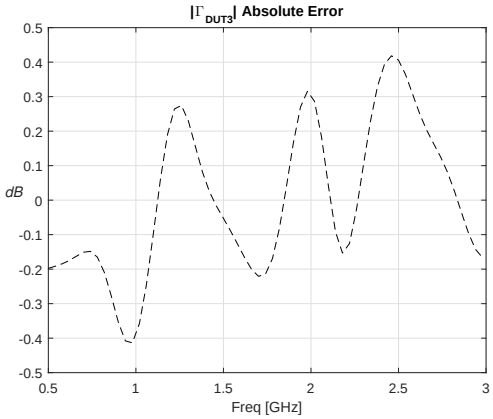

(c) magnitude absolute error

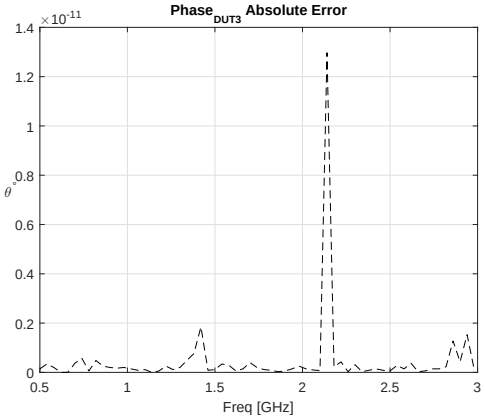

(d) phase error

Figure 3.9: 3rd DUT Simulation Results

3.4 Results Analysis

From Figures 3.5, 3.7 and 3.9, this novel calibration approach (use of S-parameters of the six-port reflectometer vs calibration standards/synthesized active loads) proved its validity. Unlike bi-linear transformation or other calibration techniques used to calibrate six-port reflectometers, measurements of S-parameters of the designed circuit provide means to confirm design's parameter – M_i and q_i, a less complicated calibration procedure, and minimal systematic error for calibration. The simulated results shown above in the figures demonstrated that the design of six-port reflectometer performed with an absolute error of approx. 0.2 dB in $|\Gamma_{DUT}|$ with zero error in phase over the entire simulated bandwidth.

The results from ADS simulation supported this thesis' goal to investigate six-port reflectometer based VNA with separate and independent RF power sources. The next chapter focuses on the theory of calibration of dual six-port reflectometer and simulated results of two-port networks' DUTs.

Chapter 4

Six-Port Network Analyzer

In the previous chapters, history, theory, designs, calibration techniques, and results of a simulated six-port reflectometer's prototype were presented. The results were encouraging to pursue and validate construction of an SPR based VNA (SPNA) through simulation with ADS. A network analyzer incorporating two six-port reflectometers was first introduced by Hoer in 1977 [33]. Incorporation of two SPRs will allow S-parameters measurements of two-port network DUTs. This chapter discusses the theory of SPNA and demonstrates simulations for Hoer's SPNA design (one power source), SPNA with independent RF power sources, and comparison of their results.

4.1 SPNA Theory and Calibration

From chapter two, the complex reflection coefficient of a DUT can be determined via scalar measurements of power using a six-port reflectometer, with no need for phase measurement. The use of two six-port reflectometers in conjunction with an appropriate calibration technique can lead to determination of four scattering parameters of any two-port DUT. Figure 4.1 shows a basic topology of a vector network analyzer using two six-port reflectometers with two attenuators, i.e. A_1 and A_2, and phase shifter to control the amplitude and phase of the merging RF signals, a_1 and a_2, into the two testing planes.

When the RF signals are applied to both reflectometers simultaneously, SPR# 1 and

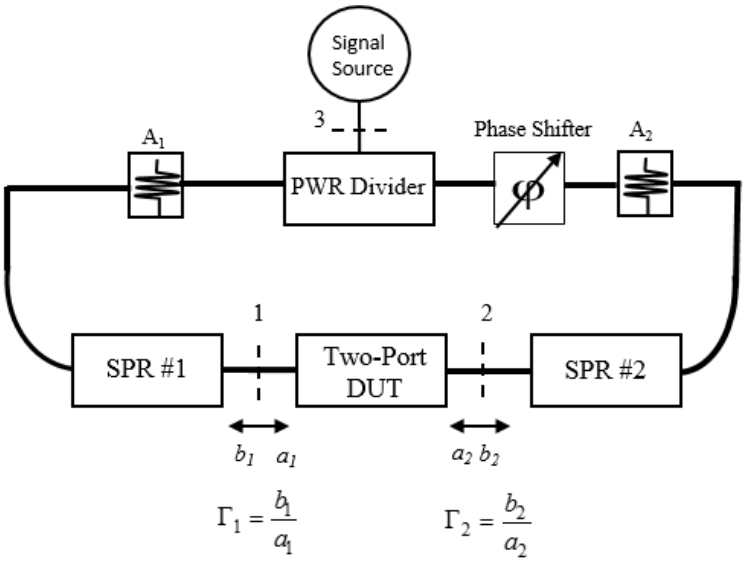

Figure 4.1: Basic topology of a six-port network analyzer (SPNA)

SPR# 2 will measure the complex ratios

$$\Gamma_1 = \frac{b_1}{a_1} \tag{4.1}$$

$$\Gamma_2 = \frac{b_2}{a_2} \tag{4.2}$$

where Γ_1 and Γ_2 are not reflection coefficients in the normal sense, but simply relate two traveling waves in opposite directions. These two ratios are related by the S-parameters of the two–port DUT [13, 33]. To derive the expression for the S-parameters of a two-port DUT, one can let

$$b_1 = S_{11}a_1 + S_{12}a_2 \tag{4.3}$$

$$b_2 = S_{21}a_1 + S_{22}a_2 \tag{4.4}$$

and dividing equation (4.3) by a_1, and equation (4.4) by a_2, yields

$$\Gamma_1 = \frac{b_1}{a_1} = S_{11} + S_{12}\frac{a_2}{a_1} \tag{4.5}$$

$$\Gamma_2 = \frac{b_2}{a_2} = S_{22} + S_{21}\frac{a_1}{a_2} \tag{4.6}$$

where Γ_1 and Γ_2 are the *reflection coefficients* measured by SPR #1 and SPR #2. Eliminating $\frac{a_1}{a_2}$ in (4.5) and (4.6) gives

$$\Gamma_2 S_{11} + \Gamma_1 S_{22} - \Delta = \Gamma_1 \Gamma_2 \tag{4.7}$$

where $\Delta \equiv S_{11}S_{22} - S_{12}S_{21}$.

Assuming that the DUT is reciprocal, equation (4.7) suggests that three conditions (three sets of values for the attenuators, A_1 and A_2, and the phase shifter, Φ) are required to create a linear system of equations to determine the three scattering parameters of a two-port DUT (three parameters since the DUT is reciprocal). It also shows that the values of the attenuators and the phase shifter are not required to be known nor to be sequential; one attenuator can be fixed while the other attenuator and the phase shifter are changing for the creation of three conditions. If the DUT is known to be reciprocal, complex values for S_{11} and S_{22} can be determined from Δ and the magnitude of S_{12}, or S_{21} can be determined using

$$|S_{12}|^2 = |S_{21}|^2 = |S_{11}S_{22} - \Delta| \tag{4.8}$$

or, from equation (4.7),

$$|S_{12}|^2 = |S_{21}|^2 = |(\Gamma_1 - S_{11})(\Gamma_2 - S_{22})| \tag{4.9}$$

Similarly, if the reciprocity of a DUT is unknown, S_{12} and S_{21} magnitudes can be determined from (4.5) and (4.6) to be

$$|S_{12}| = |\Gamma_1 - S_{11}|\left|\frac{a_1}{a_2}\right| \tag{4.10}$$

$$|S_{21}| = |\Gamma_2 - S_{22}|\left|\frac{a_2}{a_1}\right| \tag{4.11}$$

where the values for a_1 and a_2 can be determined from the procedure described in the next section.

4.1.1 S_{21} & S_{12} Phase Analysis

For reciprocal and non-reciprocal DUTs, $\frac{a_2}{a_1}$ plays a big role in determining the phase of S_{21} and S_{12}. For either case of reciprocity, equations (4.5) and (4.6) gives

$$\psi_{12} = \psi_1 - \psi_a \tag{4.12}$$

$$\psi_{21} = \psi_2 + \psi_a \tag{4.13}$$

where ψ_{12} and ψ_{21} are the phase for S_{21} and S_{12}, respectively, and

$$\psi_1 \equiv arg(\Gamma_1 - S_{11}) \tag{4.14}$$

$$\psi_2 \equiv arg(\Gamma_2 - S_{22}) \tag{4.15}$$

$$\psi_a \equiv arg(\frac{a_2}{a_1}) \tag{4.16}$$

where the angles ψ_1 and ψ_2 are known; however, since the six-port reflectometer does not directly measure the ratio $\frac{a_2}{a_1}$ to determine ψ_a, further analysis is required.

When a DUT is *reciprocal*, (4.12) and (4.13) can be solved for ψ_a and $\psi_{12} = \psi_{21}$ to be [12, 31]

$$\psi_{12} = \psi_{21} = \frac{\psi_1 + \psi_2}{2} + n\pi \tag{4.17}$$

$$\psi_a = \frac{\psi_1 - \psi_2}{2} + n\pi \tag{4.18}$$

where the ambiguity $n\pi$ arises from dividing by 2, and n is an integer. The value of n can be

determined via good estimate of ψ_{12} or ψ_a. Hoer suggests that the value of n can be resolved through a good estimate of ψ_{12} or ψ_a, by using equations derived from non-reciprocal DUT case ($\psi_{12} \neq \psi_{21}$) [33].

From Figure 4.1, the three terminal planes whose ports are 1, 2 and 3 one can show that

$$\frac{a_2}{a_1} = (s_{21} - s_{11}\frac{s_{23}}{S_{13}})\Gamma_1 - (s_{12}\frac{s_{23}}{s_{13}} - s_{22})\Gamma_1\frac{a_2}{a_1} + \frac{s_{23}}{s_{13}} \tag{4.19}$$

where s_{ji} are the scattering parameters of the three ports junction, and (4.19) can be re-written as

$$\frac{a_2}{a_1} = C_1\Gamma_1 - C_2\Gamma_2\frac{a_2}{a_1} + C_3 \tag{4.20}$$

where C_1, C_2 and C_3 are corresponding terms in (4.19) and (4.20). Solving for $\frac{a_2}{a_1}$ yields

$$\frac{a_2}{a_1} = \frac{C_3 + C_1\Gamma_1}{1 + C_2\Gamma_2} \tag{4.21}$$

To determine the values for C_1, C_2 and C_3 needed to solve for ψ_a, three standards are required. One of those standards can be of *"zero electrical length"* (i.e. connecting measurement planes 1 and 2 directly to each other), and the other two standards can be matched to the circuit with approximately same electrical length [33]. Once C_1, C_2 and C_3 are calculated, ψ_a and n is determined for S_{21} and S_{12} phase values.

4.2 SPNA Simulations and Results

To simulate the SPNA, two designs were considered; these are Hoer's original SPNA design and SPNA with an independent RF power sources (see Figures 4.2 and 4.3). In simulating either designs, there was no impact of the attenuators' values (i.e. A_1 and A_2) to the measurements and the calibration procedures, thus they were not considered during the simulation, nor incorporated in the physical realization of the prototype.

The procedure to simulate and compute the S-parameters for a two-port network DUT is once the DUT is placed on the measuring plane, three sets of measurements of the four power probes for each SPR are recorded over the entire simulation's frequency. These three sets of measurements will have to be under different conditions, i.e. one or both RF power sources provide different RF signal phase than the other. Once these three power measurements are recorded, computation of Γ_{1i} and Γ_{2i} (where 1 and 2 indicate the SPR and $i = 1, 2,$ and 3 for conditions) is completed and recorded for each condition, and finally Γ_{1i} and Γ_{2i} are used to compute solutions for S_{11}, S_{21}, and S_{22} using equation (4.7). It is important for the reader to know that the values for F_i, E_i, and H_i for each SPR must already been computed and recorded to be used in the computation for Γ_{1i} and Γ_{2i}, and that this thesis assumes all DUTs are reciprocal, hence only S_{21} values were computed.

The simulation of both designs was done using two DUTs, which were designed arbitrarily. Those DUTs were constructed in ADS with arbitrarily configuration using microstrip lines, capacitors, and resistors. The values for those DUTs' components were chosen arbitrarily, and were based on different substrate and thickness than the ones used to design the SPRs. See Figures 4.4 and 4.5.

The three sets of measurements were conducted using an arbitrary RF power phase; for the first DUT's set of measurements, the RF power source's phase was set to $60°$, $120°$, and $180°$, while the second DUT's were set to $90°$, $225°$, and $315°$. The RF power source for

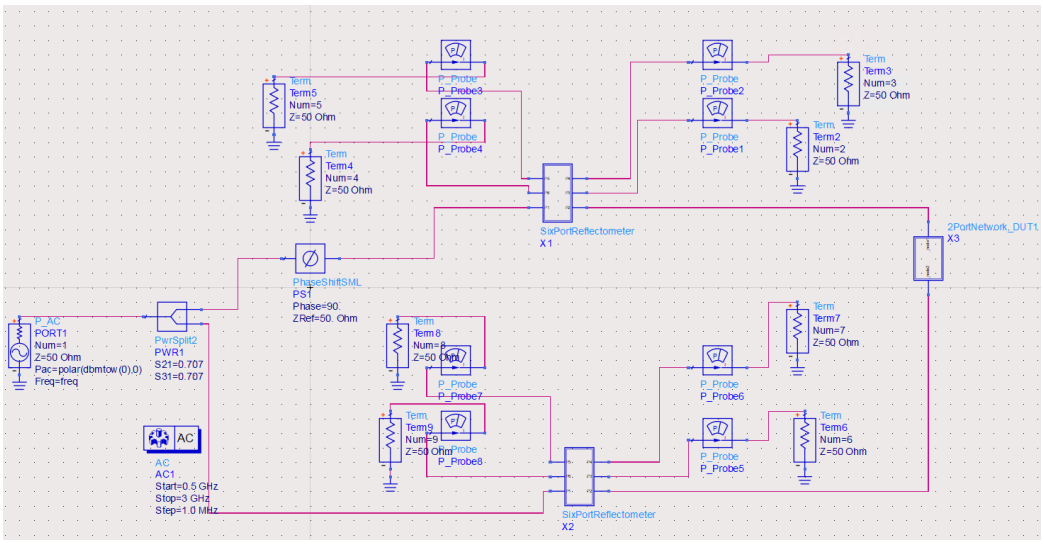

Figure 4.2: Hoer's original SPNA design setup in ADS

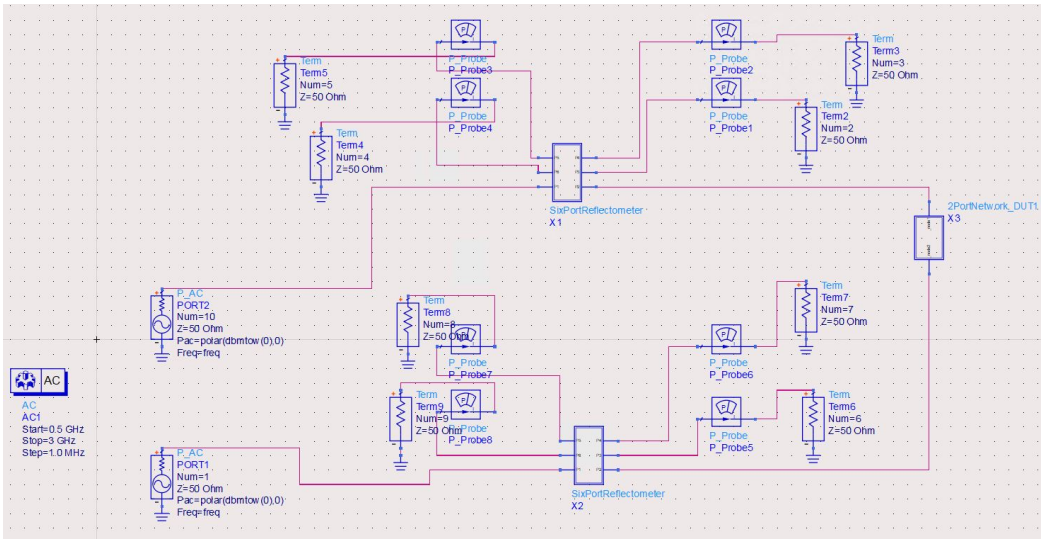

Figure 4.3: SPNA with independent RF power sources design setup in ADS

Hoer's design simulation was kept at 0 dBm for all the sets of measurements, while the independent RF power sources for this thesis objective were set differently; one was set at 0 dBm, and the other at -10 dBm. This to simulate the fact that not all RF power sources would provide identical RF signal and to show that different power level of the signal will still provide good results.

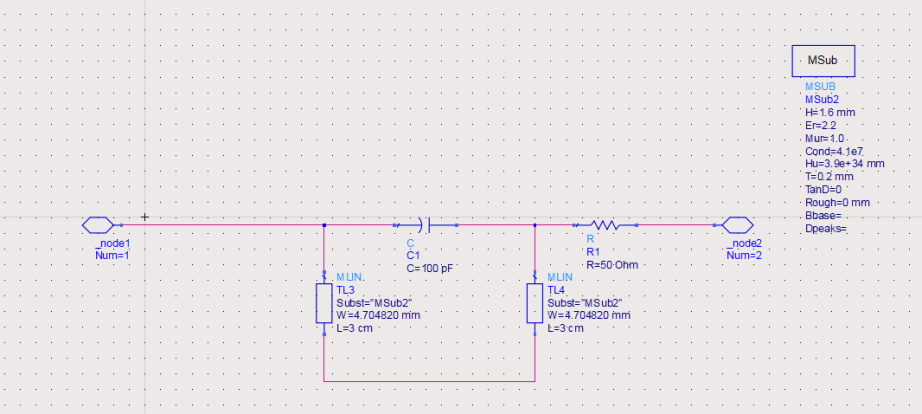

Figure 4.4: 1st 2-Port Network DUT

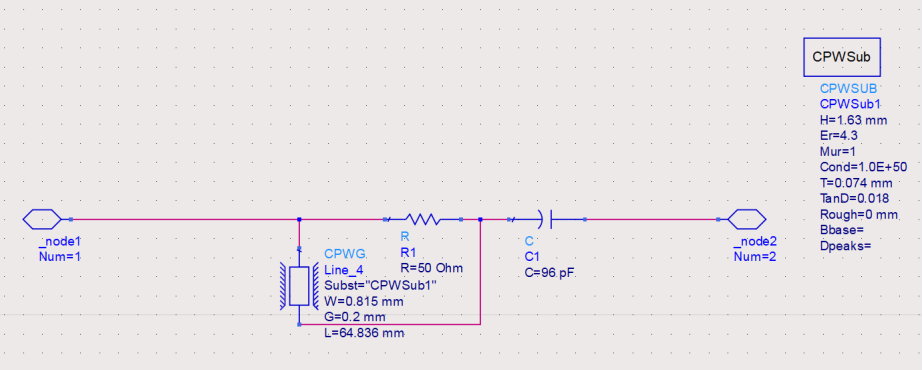

Figure 4.5: 2nd 2-Port Network DUT

4.3 Results

As stated in the previous section, two DUTs were designed in ADS, and both Hoer's and independent RF power sources were simulated to collect power measurements and compare results. In the following subsection, results for S_{11}, S_{21}, and S_{22} are compared between the two designs, as well as their absolute error in comparison to their true values (Gamma True), over simulation frequency range of 0.5–3 GHz. It is important for the reader to know that plots for magnitude and phase were plotted using Matlab code for every 10^{th} point in order to distinguish the plotted lines. However, Absolute error plots were plotted using all points of the results.

4.3.1 Results using 1st DUT

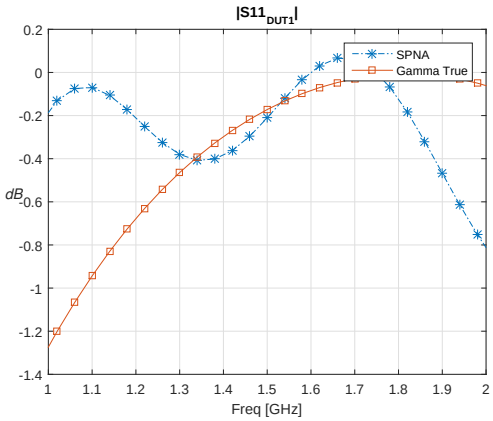

(a) S_{11} magnitude independent RF power sources

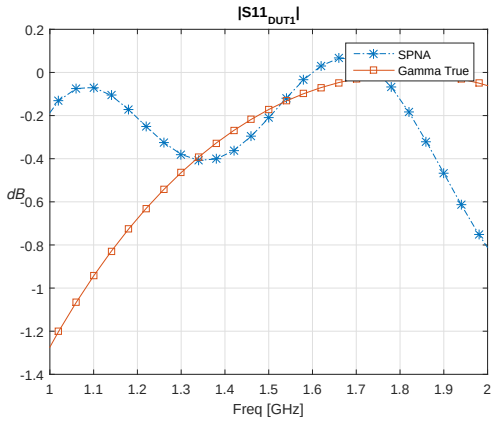

(b) S_{11} magnitude Hoer's design

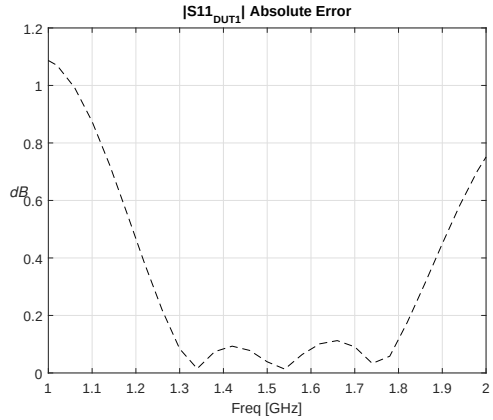

(c) Absolute error for independent RF power sources

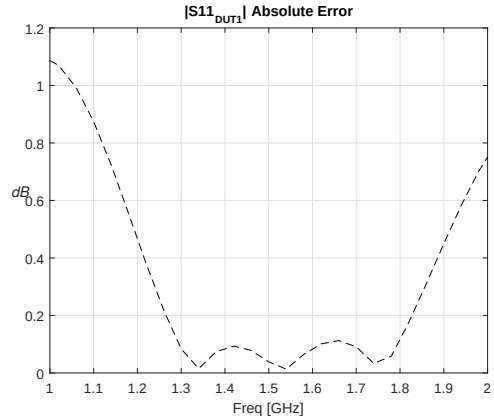

(d) Absolute error for Hoer's design

Figure 4.6: 1st two-port DUT S_{11} magnitude simulation results

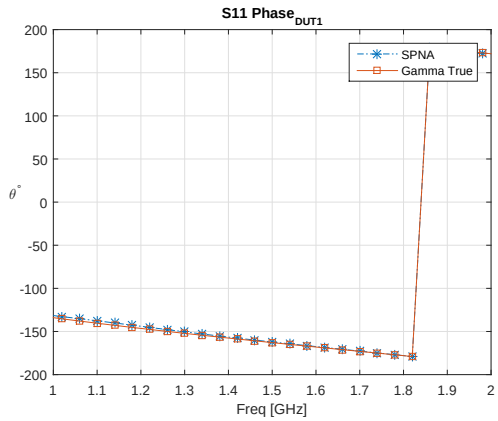

(a) S_{11} phase independent RF power sources

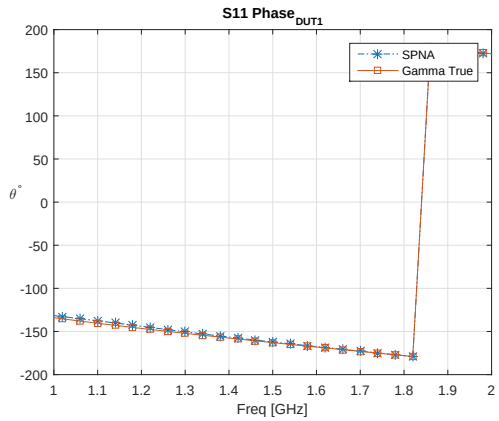

(b) S_{11} phase Hoer's design

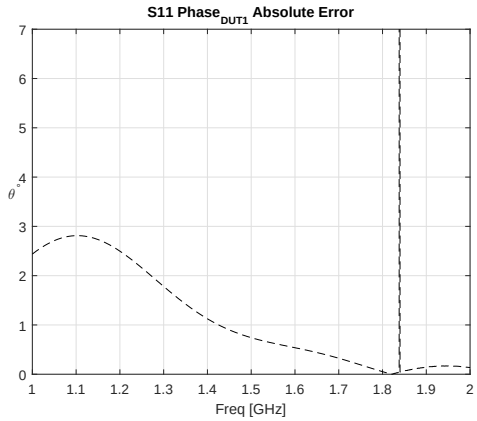

(c) Absolute error for independent RF power sources

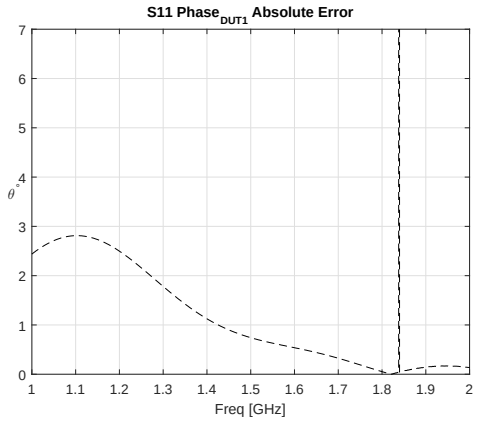

(d) Absolute error for Hoer's design

Figure 4.7: 1st two-Port DUT S_{11} phase simulation results

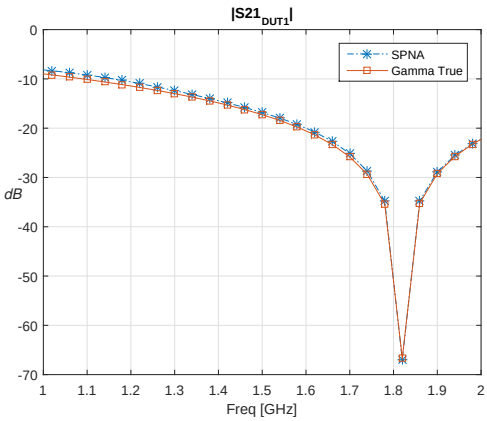

(a) S_{21} magnitude independent RF power sources

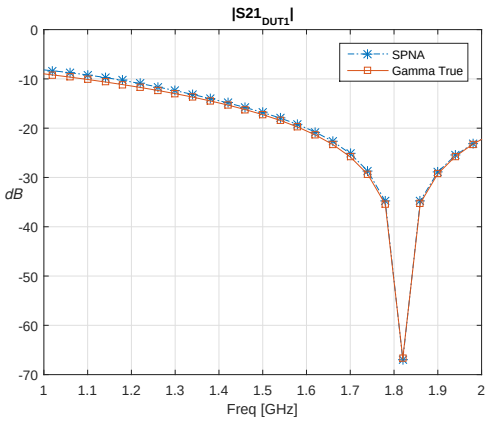

(b) S_{21} magnitude Hoer's design

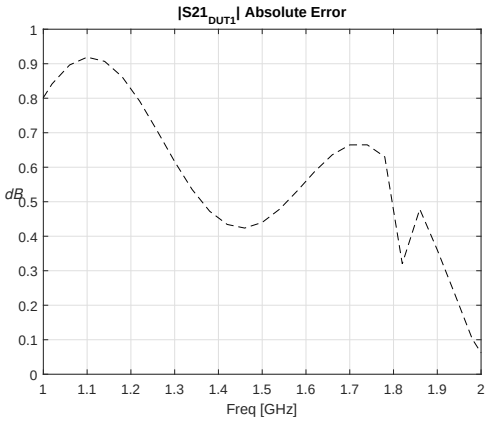

(c) Absolute error for independent RF power sources

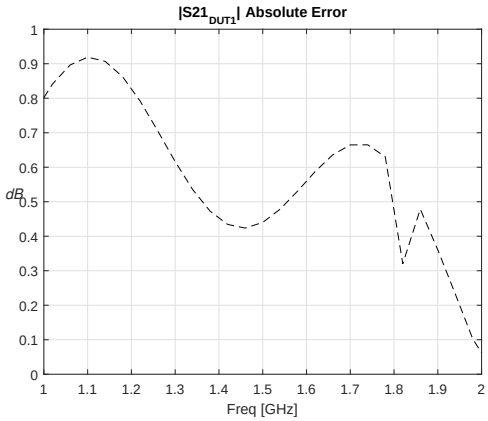

(d) Absolute error for Hoer's design

Figure 4.8: 1st two-port DUT S_{21} magnitude simulation results

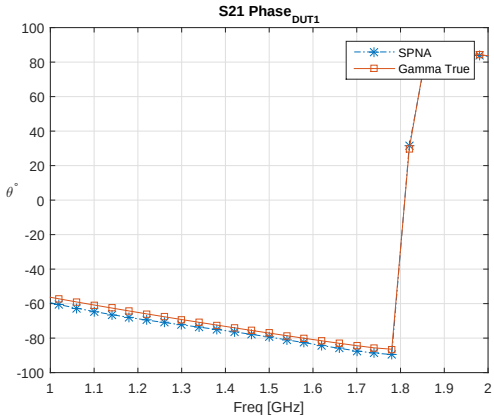

(a) S_{21} phase independent RF power sources

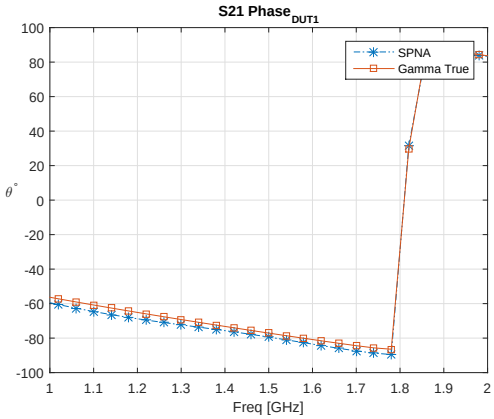

(b) S_{21} phase Hoer's design

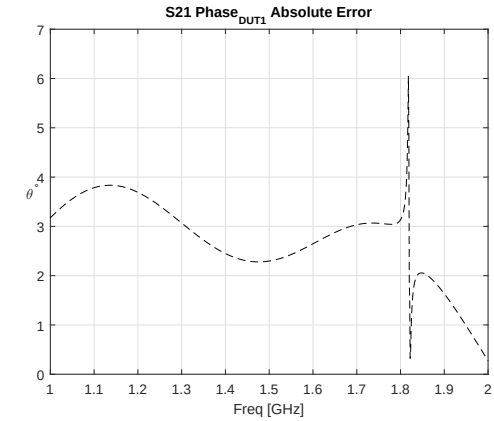

(c) Absolute error for independent RF power sources

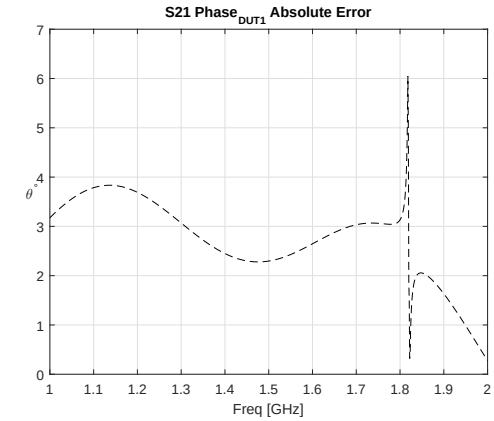

(d) Absolute error for Hoer's design

Figure 4.9: 1st two-port DUT S_{21} phase simulation results

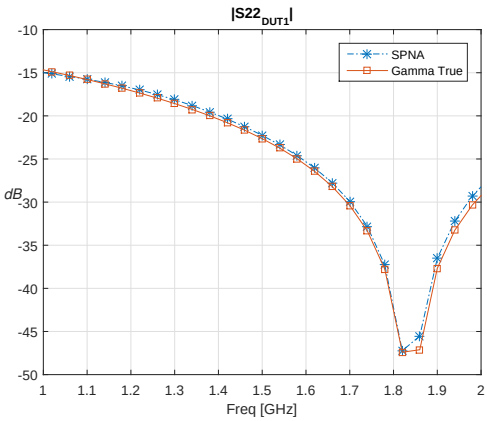

(a) S_{22} magnitude independent RF power sources

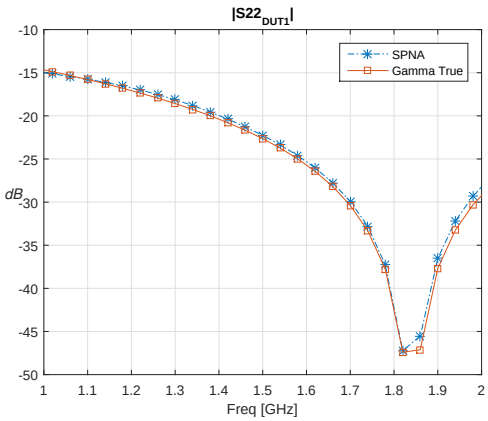

(b) S_{22} magnitude Hoer's design

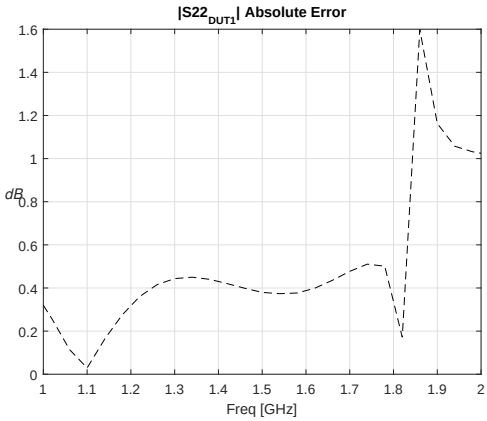

(c) Absolute error for independent RF power sources

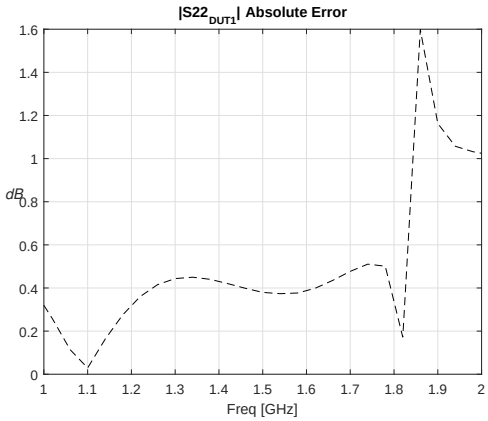

(d) Absolute error for Hoer's design

Figure 4.10: 1st two-port DUT S_{22} magnitude simulation results

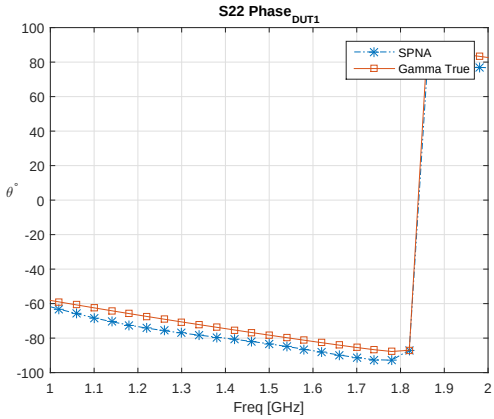

(a) S_{22} phase independent RF power sources

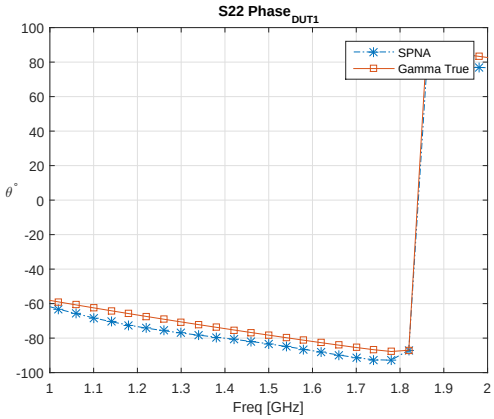

(b) S_{22} phase Hoer's design

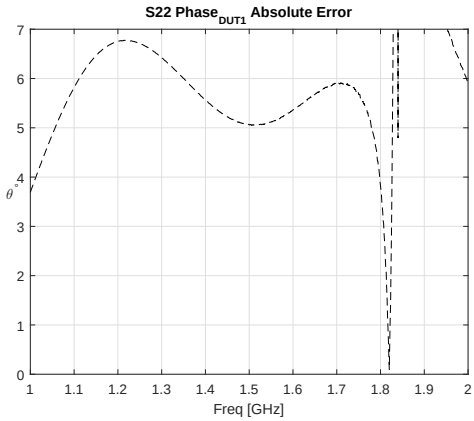

(c) Absolute error for independent RF power sources

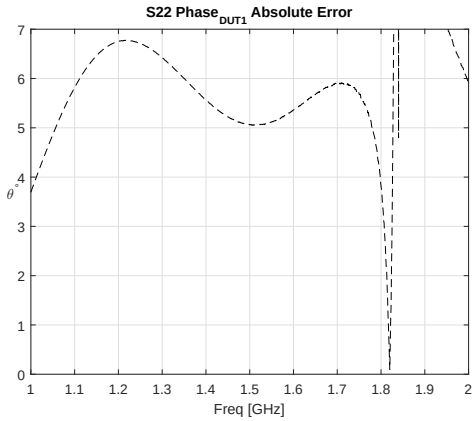

(d) Absolute error for Hoer's design

Figure 4.11: 1st two-port DUT S_{22} phase simulation results

4.3.2 Results using 2nd DUT

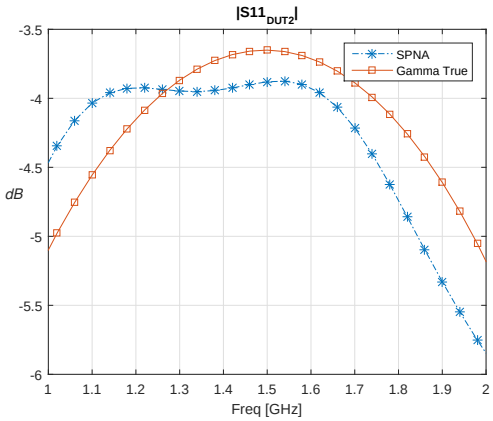

(a) S_{11} magnitude independent RF power sources

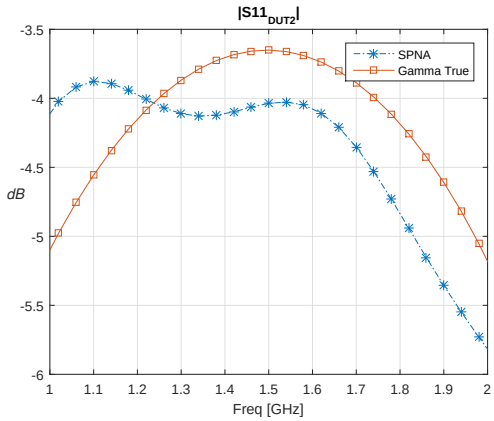

(b) S_{11} magnitude Hoer's design

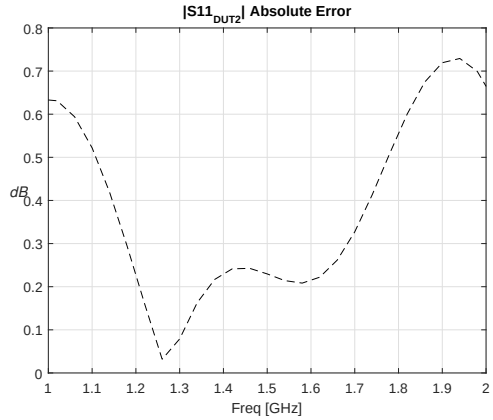

(c) Absolute error for independent RF power sources

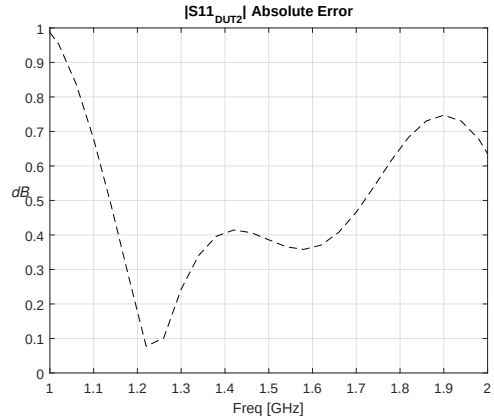

(d) Absolute error for Hoer's design

Figure 4.12: 2nd two-port DUT S_{11} magnitude simulation results

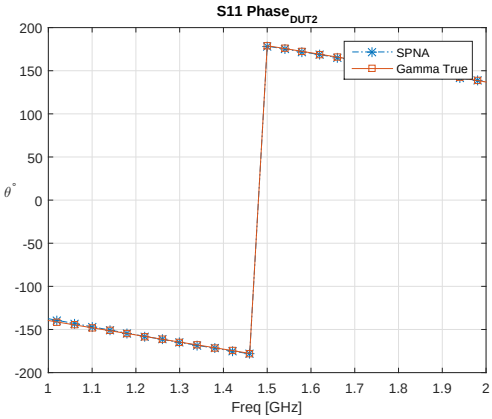

(a) S_{11} phase independent RF power sources

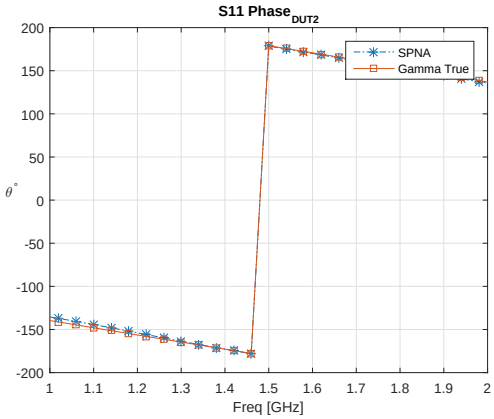

(b) S_{11} phase Hoer's design

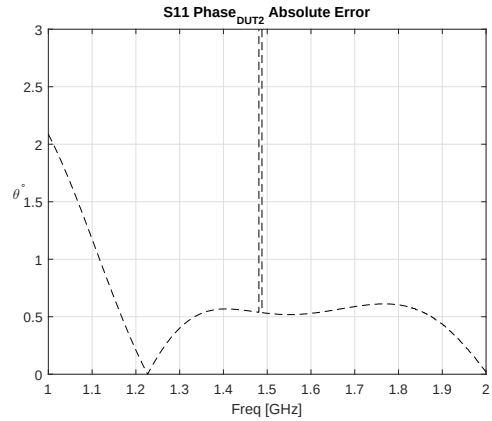

(c) Absolute error for independent RF power sources

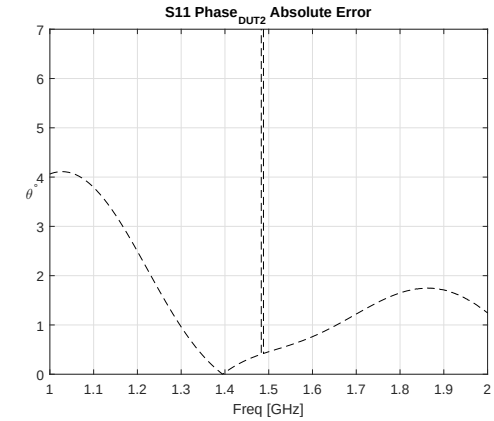

(d) Absolute error for Hoer's design

Figure 4.13: 2nd two-port DUT S_{11} phase simulation results

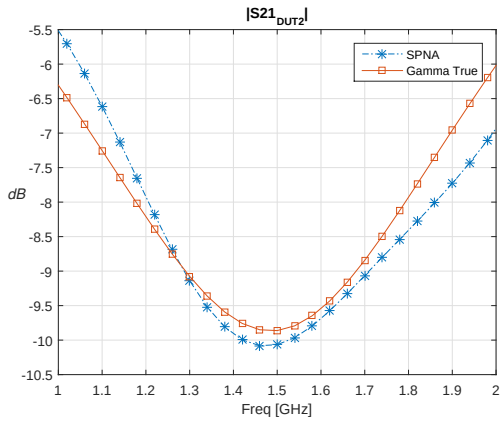

(a) S_{21} magnitude independent RF power sources

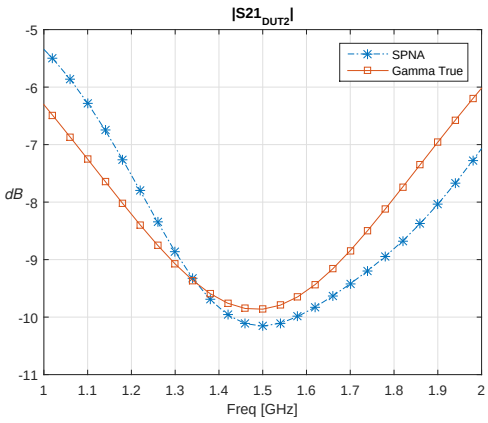

(b) S_{21} magnitude Hoer's design

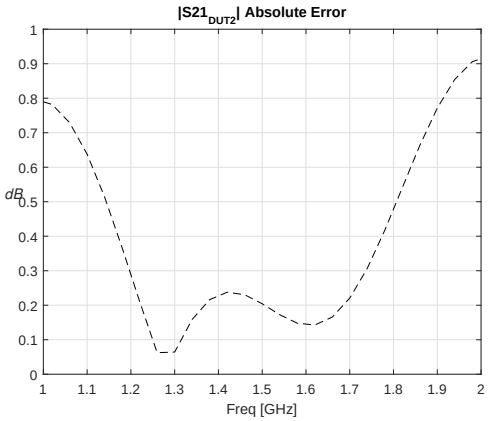

(c) Absolute error for independent RF power sources

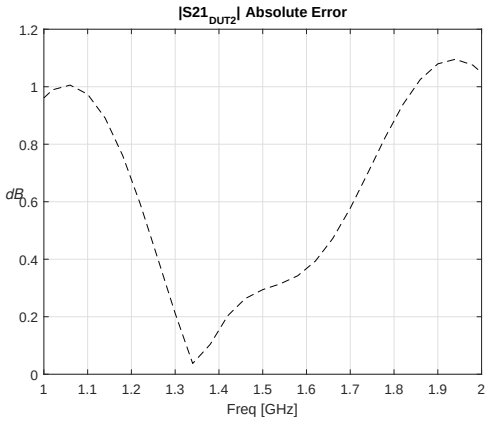

(d) Absolute error for Hoer's design

Figure 4.14: 2nd two-port DUT S_{21} magnitude simulation results

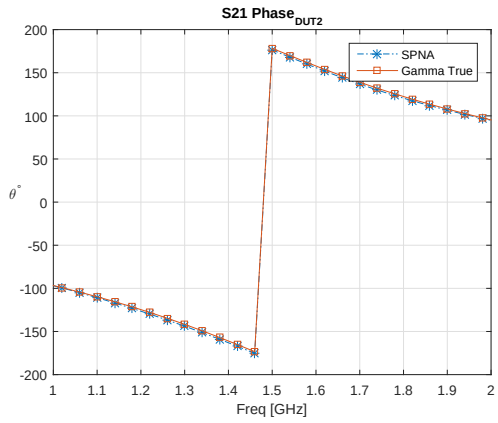

(a) S_{21} phase independent RF power sources

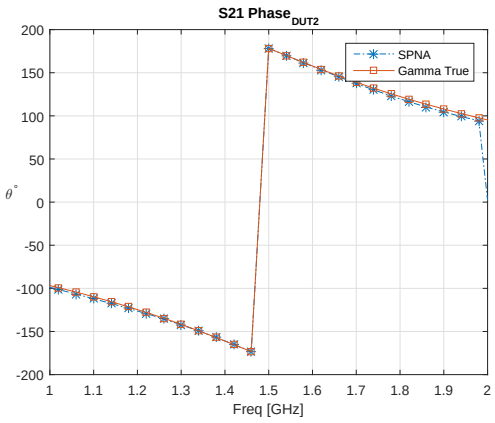

(b) S_{21} phase Hoer's design

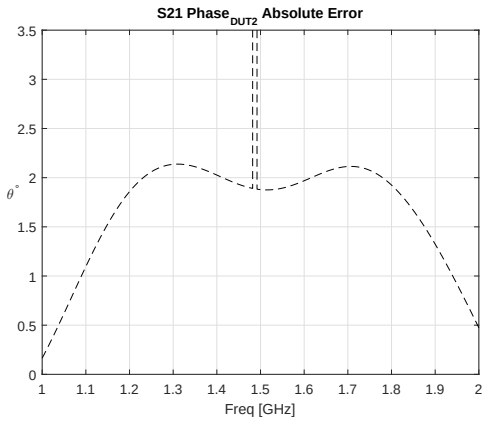

(c) Absolute error for independent RF power sources

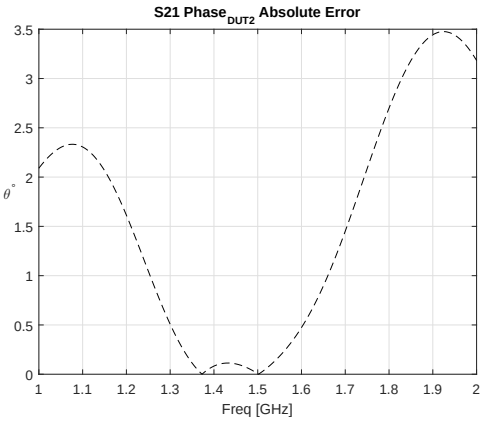

(d) Absolute error for Hoer's design

Figure 4.15: 2nd two-port DUT S_{21} phase simulation results

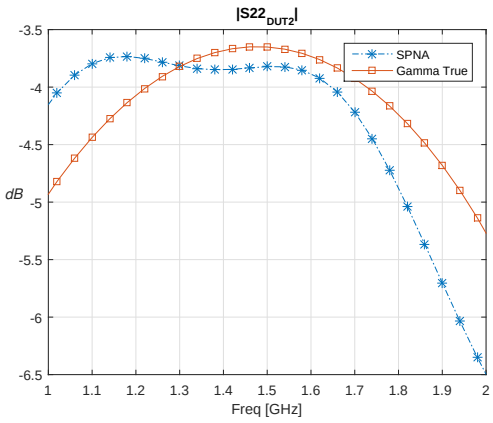

(a) S_{22} magnitude independent RF power sources

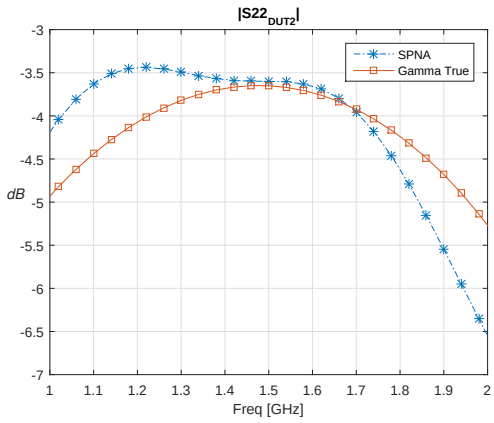

(b) S_{22} magnitude Hoer's design

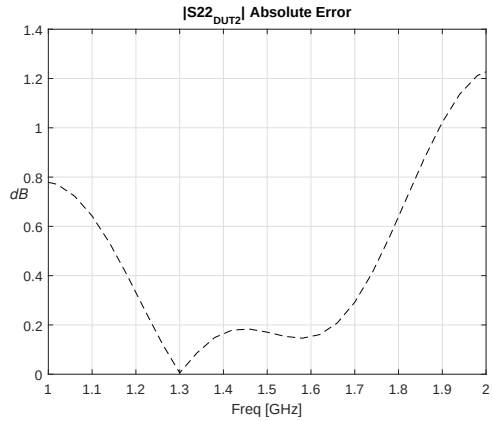

(c) Absolute error for independent RF power sources

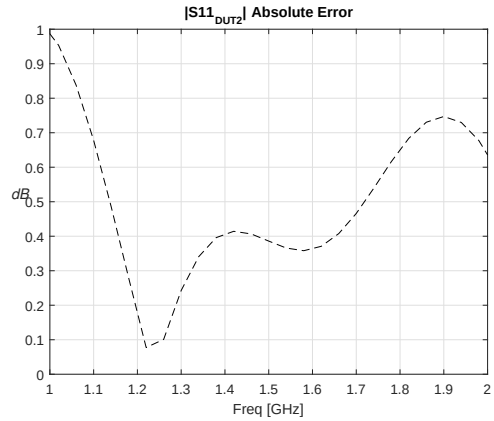

(d) Absolute error for Hoer's design

Figure 4.16: 2nd two-port DUT S_{22} magnitude simulation results

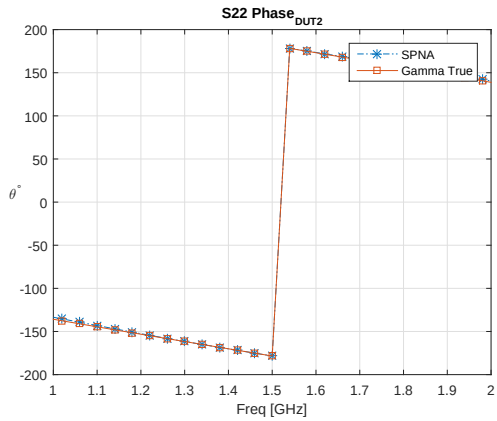

(a) S_{22} phase independent RF power sources

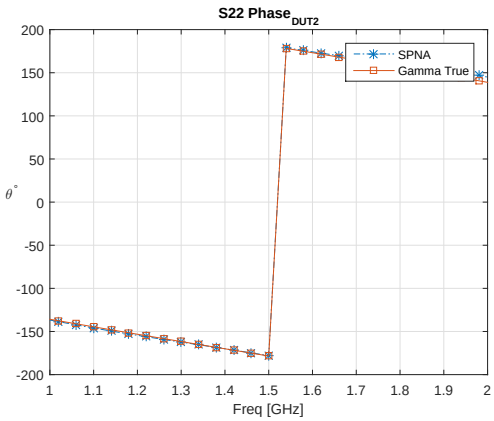

(b) S_{22} phase Hoer's design

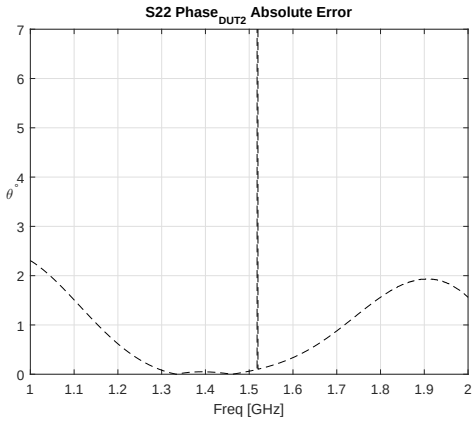

(c) Absolute error for independent RF power sources

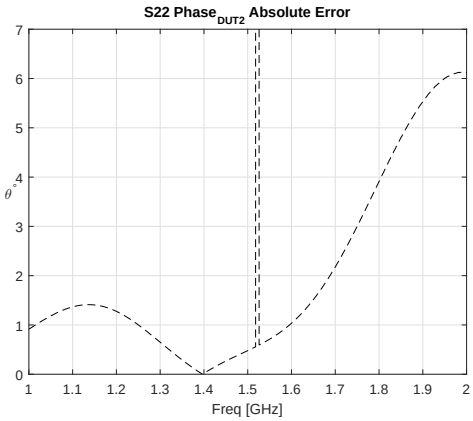

(d) Absolute error for Hoer's design

Figure 4.17: 2nd two-port DUT S_{22} phase simulation results

4.4 Results Analysis

From subsection 4.3.1 and 4.3.2, the results were in agreement between the independent oscillator's and Hoer's design. For the first two-port DUT, both S_{11}'s and S_{22}'s absolute error were approx.0.5 dB error in magnitude, and mean of $3°$ error in phase. The values of absolute error for S_{21} were approx. 0.5 dB in magnitude, and mean of $4°$ error in phase. The same error values are true for the second DUT. These results were computed without conducting additional calibration procedure for S_{21} phase descried in sub-section 4.0.1.

This demonstrate that the main research objective of this thesis was confirmed; SPR based VNA with independent RF power sources can provide acceptable values for two-ports DUT's S-parameters in comparison to Hoer's original design. These simulated results also prove that specific calibration technique of the designed SPR is valid. The simulated results for SPNA are encouraging to implement a physical prototype.

Chapter 5

Physical Realization of SPNA

In chapters three and four, the results of simulating SPR and SPNA of the chosen design were presented and proven valid for an implementation of an SPNA with independent RF power sources. Those results were encouraging to implement a physical prototype for the SPNA. This chapter will discuss the process of implementing the physical prototype of the chosen SPR design, including designing the prototype's printed circuit board (PCB) with Altium Design software, physical circuit, calibration and measurement's setup, and result's analysis.

5.1 PCB design and Physical Circuit

The physical prototype was modeled using Altium Design Software. The circuit was designed using FR4 substrate with relative permittivity, $\epsilon_r = 4.3$, and coplanar waveguide with line dimensions of $H = 1.6$ mm for substrate thickness, $W = 0.815$ mm for conductor's width, and $G = 0.2$ mm for gap width between the conductors and the ground plates with copper or conductor's thickness $T = 35.56$ um. A testing line was included within the PCB to test the manufacturer's accuracy for line's impedance control, $Z_o = 50\Omega$, with length of 90.5 mm. See Figure 5.1 for the SPR prototype's PCB layout and connecting line lengths.

Table 5.1 shows the main MIC components used to implement the physical prototype of the SPR. Other components such as resistors, capacitors and subminiature version A (SMA) connectors, although were not mentioned here have been used to complete the prototype.

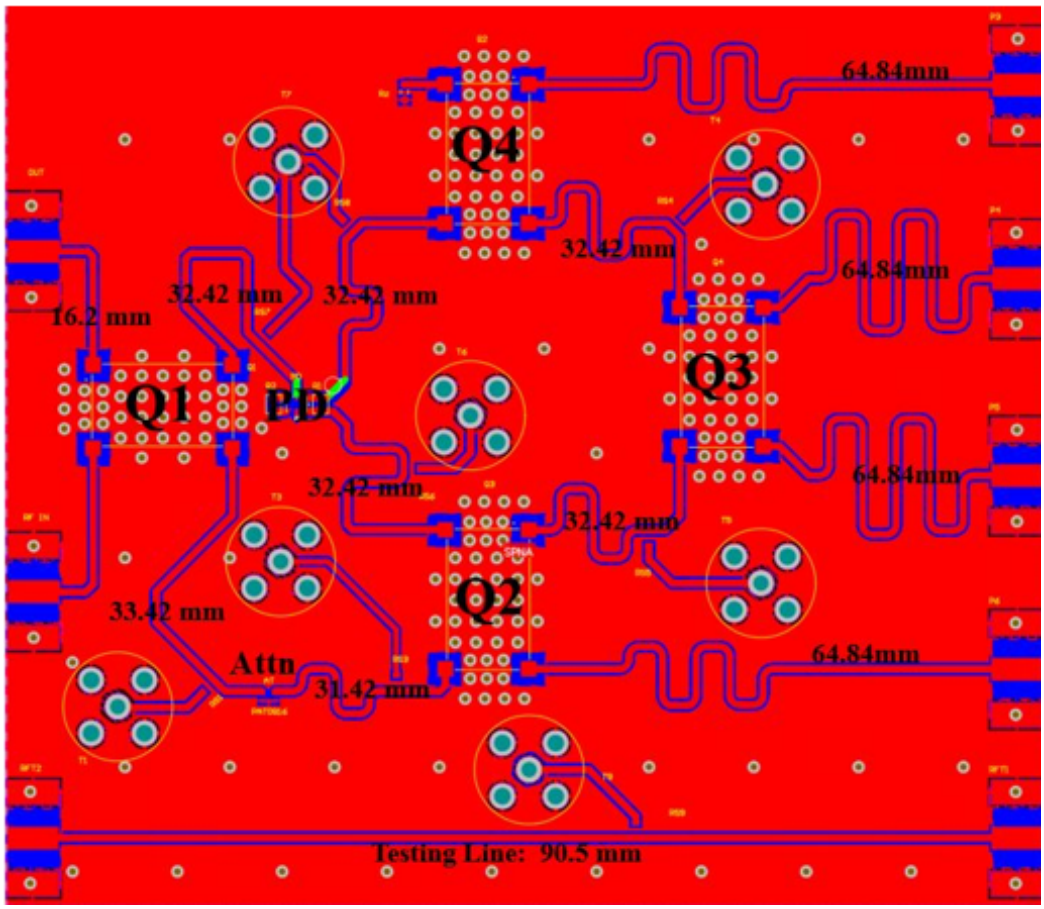

Figure 5.1: Six-port reflectometer prototype PCB layout

Table 5.1: MIC components used in six-port reflectometer physical prototype

3dB–90° Hybrid Coupler: Anaren model 11035-3S					
Freq [GHz]	Isolation [dB]	Insertion Loss [dB]	Phase Balance [degrees]	Amp Balance [dB]	VSWR
1.0-2.0	20	0.45	±3	±0.55	1.3:1
Wilkinson's Power Divider:Anaren model PD0922J5050S2HF					
Freq [GHz]	Isolation [dB]	Insertion Loss [dB]	Phase Balance [degrees]	Amp Balance [dB]	In/Out [W]
0.95-2.15	12	0.7-0.8	1.0-3.0	0.1-0.5	50/50
Attenuator : Analog Devices model HMC653LP2E					
Atten. Value [dB]	VSWR [∼6GHz]	Atten. Tolerance	Operating Temp [°C]	Power Handling [dBm]	Freq [GHz]
3	<1.3	± 0.3	-55 – +125	up to 20	DC–10

A photograph of the final circuit for the SPR prototype is shown in Figure 5.2.

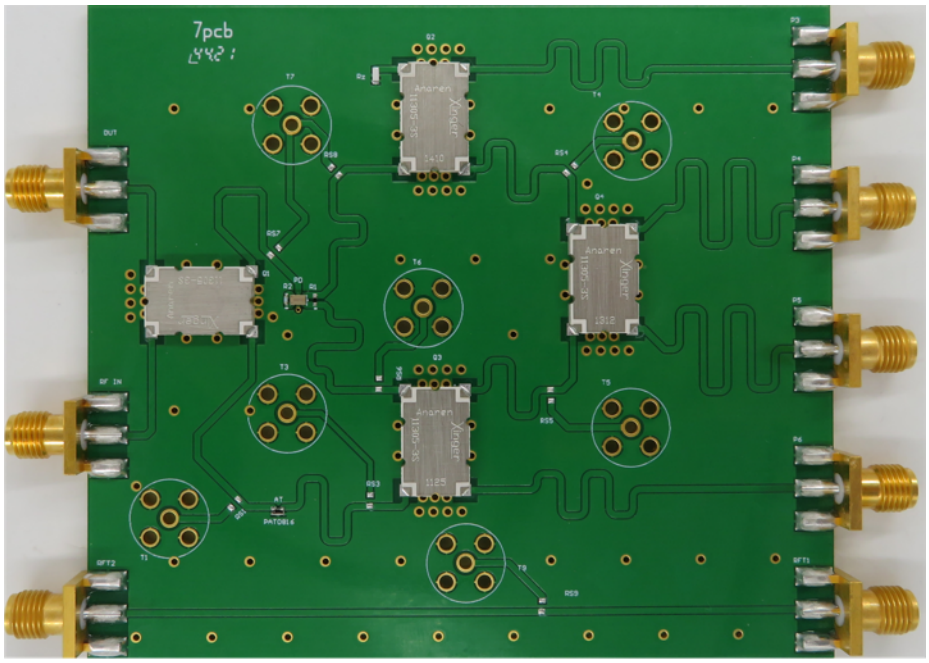

Figure 5.2: Six-port reflectometer prototype

5.2 Measurements setup

To confirm the prototype's performance, measurements confirming that connecting lines were manufactured to the specifications (i.e., $Z_o = 50\Omega$ and $\theta = 180°$ for electrical length at center frequency, $f_c = 1.5$ GHz), as well as the 3 dB couplers are operating in accordance with its data sheet, are essential. Furthermore, measurements of the prototype S-parameters are required to confirm agreement of the prototype's q_i values with the simulated values.

To conduct these measurements, we used the readily available 24 port VNA in the EIL lab to measure the prototype's S-parameters for the computation of q_i and M_i. Furthermore, the 24 port VNA was also utilized as means of collecting scalar power measurements at ports 3, 4, 5, and 6 from each SPR. To confirm this approach, simulated power measurements setup was developed in ADS using solely S-parameters, Figure 5.3. The power measurements were collected using the magnitude values of $|S_{21}|^2$ to represents the power

measurement for port 3, $|S_{31}|^2$ to represents the power for port 4, $|S_{41}|^2$ to represents the power for port 5, and $|S_{51}|^2$ to represents the power for port 6.

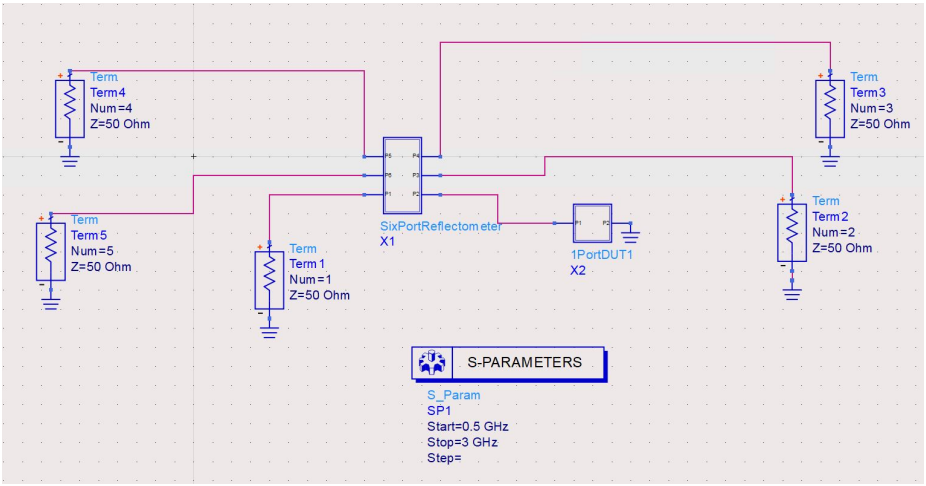

Figure 5.3: Six-port reflectometer prototype

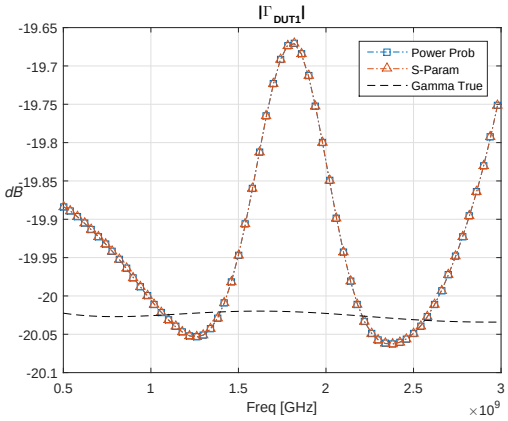

(a) S_{11} comparing magnitudes of DUT1

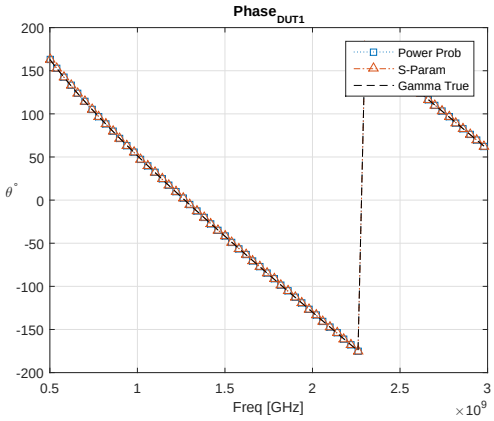

(b) S_{11} comparing phases of DUT1

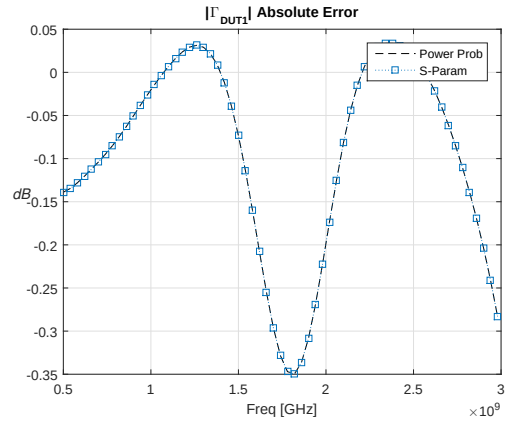

(c) comparing absolute magnitude errors

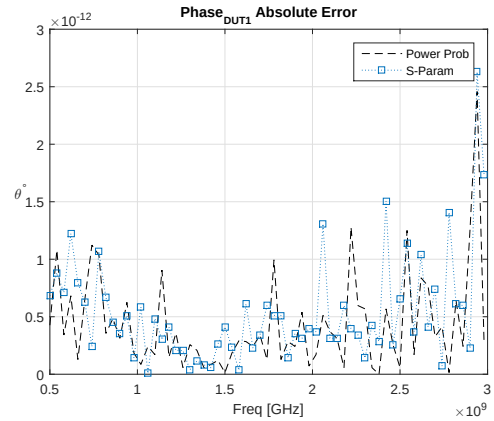

(d) comparing phase errors

Figure 5.4: 1st one-port DUT S_{11} comparison for magnitude and phase using S-parameters as means for power measurements

Figure 5.4 demonstrates a comparison between simulated results using power probs and the ADS S-parameters simulator as means for power measurements. It is clear that this approach is valid to collect the data required (i.e. power measurements) to confirm the performance of the SPR prototype.

5.3 Results Analysis

Four SPR prototype PCBs were built, and measurements of S-parameters using the 24 port VNA were done to compute the q_i points and compare those to the ones from ADS simulations, Figure 2.15. From Figures 5.5 and 5.6, we can clearly see that the experimental q_is differ somewhat from the expected values of simulated q_i (Figure 2.15) over a BW of approx. 500 MHz (0.9 –1.4 GHz). This is due to the non ideal behavior of the MIC components (couplers, power divider) as well as the characteristic impedance of the lines in the PCB only being close to the nominal 50 ohms in this BW. Figure 5.7 shows comparison between the measured and simulated Z_o of the testing line, or trace.

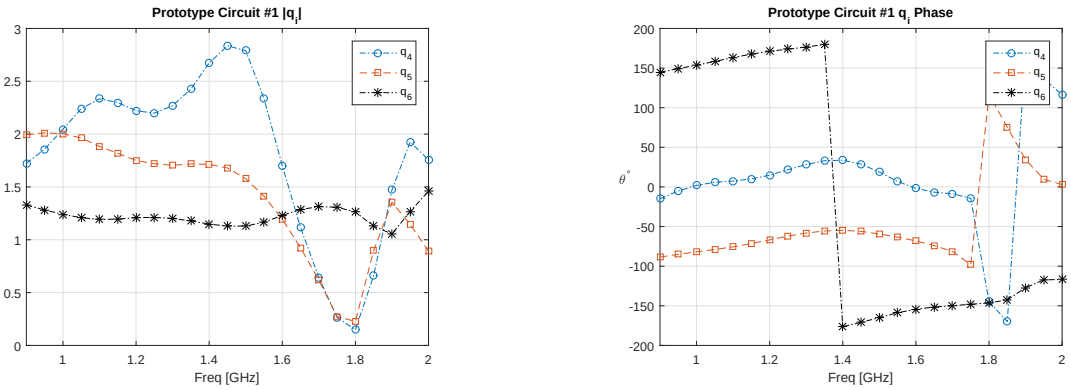

(a) Prototype Circuit 1 q_i Magnitude (b) Prototype Circuit 1 q_i Phase

Figure 5.5: q_i for physical SPR prototype circuit 1

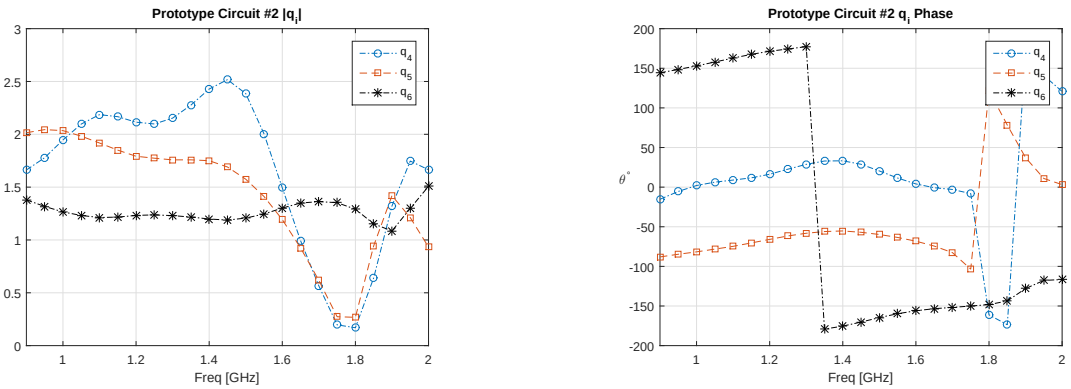

(a) Prototype Circuit 2 q_i Magnitude (b) Prototype Circuit 2 q_i Phase

Figure 5.6: q_i for physical SPR prototype circuit 2

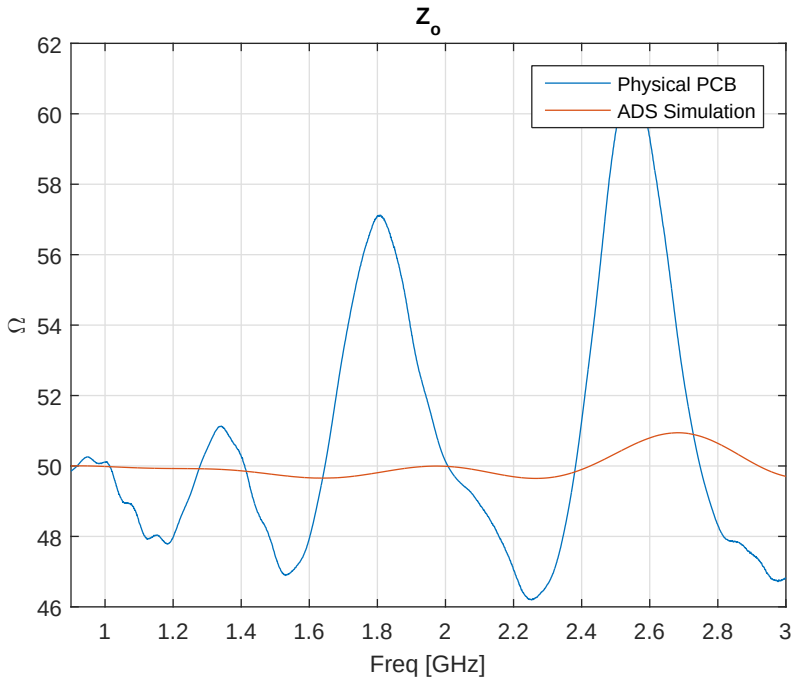

Figure 5.7: Comparison between measured and simulated values for characteristic impedance of the testing line

To confirm the operation of the PCBs (prototype circuits), a Low-Pass filter, Mini-Circuit model SLP-2400+, connected to the PCB with a thru-adaptor was used as a DUT. The Low-Pass filter has an insertion loss of 0.4 dB up to 2.2 GHz, however, adding hte thru-adapter contributed to the change in value of insertion loss to be approx. -0.5 dB over the measuring BW (0.9–1.4 GHz). As expected, best results were obtained over 500 MHz BW; this can be due to the non ideal behavior of the MIC components, lack of impedance control of the lines in the PCB (Figure 5.7), and an inconsistency of the physical length of lines in the PCBs which lead to errors in the magnitude and phase values. The reflection coefficient for the Low-Pass filter for PCB # 1 and PCB #2 are showing in Figures 5.8 and 5.9 respectively.

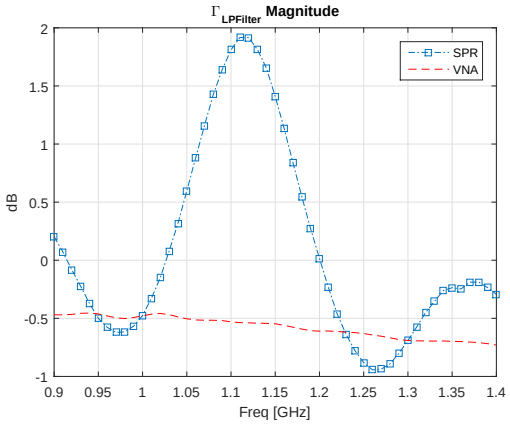

(a) Magnitude of reflection coefficient of Low-Pass Filter

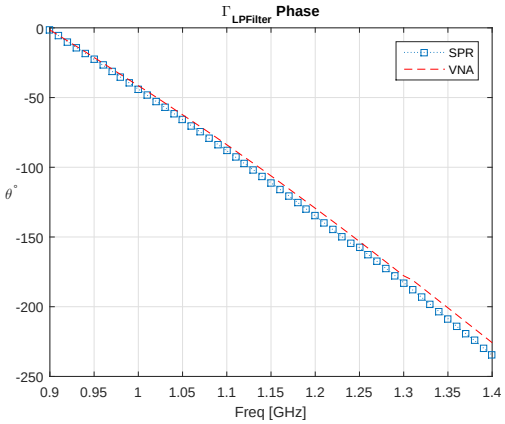

(b) Phase of reflection coefficient of Low-Pass Filter

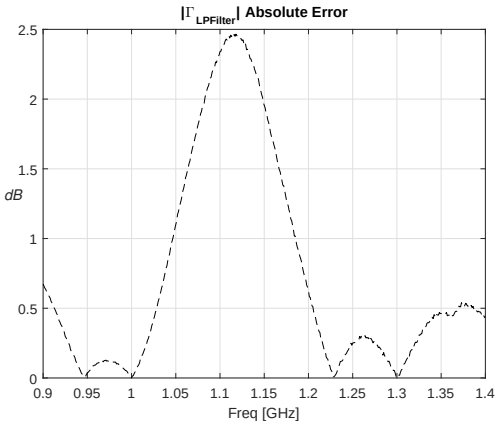

(c) Magnitude's absolute error

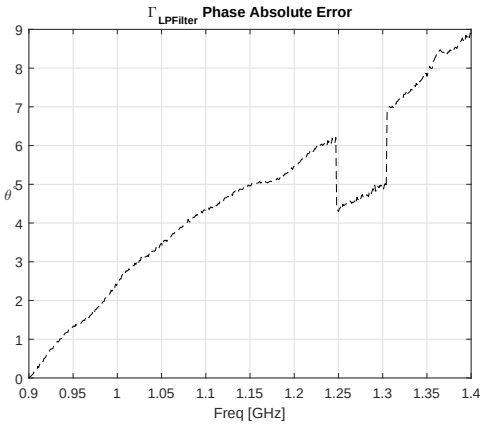

(d) Phase's absolute error

Figure 5.8: Results of Low-Pass Filterusing PCB # 1

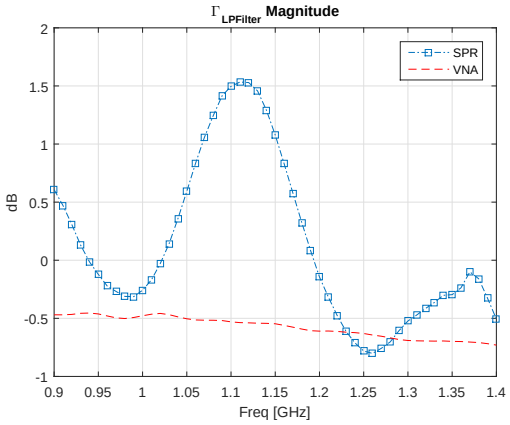

(a) Magnitude of reflection coefficient of Low-Pass Filter

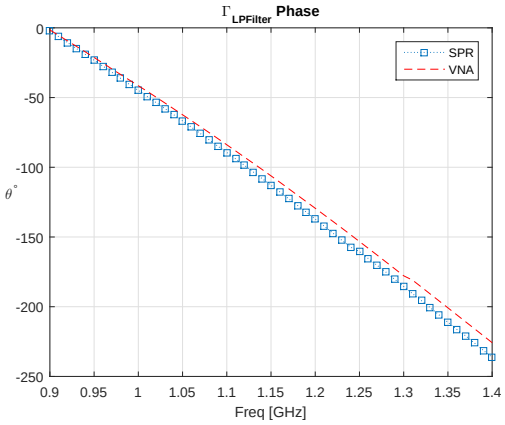

(b) Phase of reflection coefficient of Low-Pass Filter

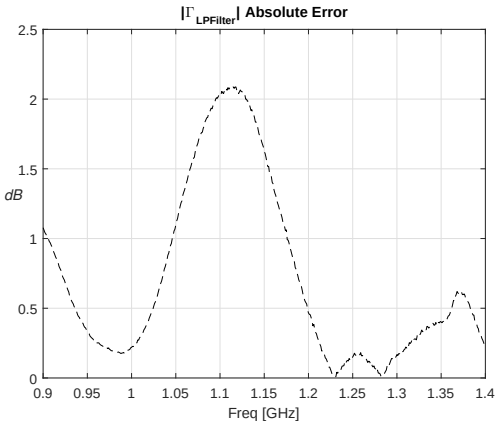

(c) Magnitude's absolute error

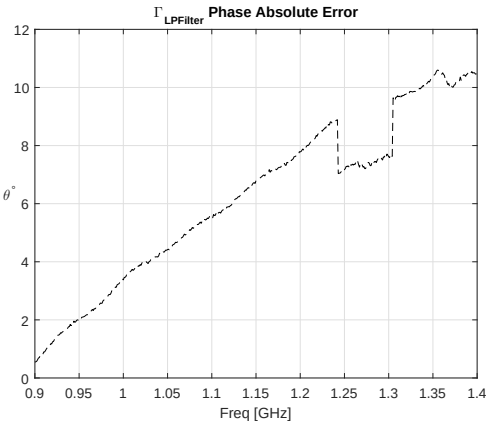

(d) Phase's absolute error

Figure 5.9: Results of Low-Pass Filter using PCB # 2

Additionally, we couldn't continue with measurements using two SPRs to confirm the main objective of this thesis; SPR based VNA (SPNA) using two independent RF power sources. This is due to the current pandemic restriction issues and the emerging of the new variant. Once the current health situation permits, efforts will be taken to confirm the results of SPNA for two-ports DUT. It is important to mention that at least one independent RF power source, in addition to the 24 port VNA, will be required to conduct the measurement's setup, and create three conditions of power measurements to compute the S-parameters of two-port network DUT

Chapter 6

Conclusion and Future Work

This thesis presented a novel use of an SPR to implement an SPNA analyzer operating with two independent RF power sources versus the traditional common RF power source and the use of attenuators and phase shifter. The main goal of this thesis was to implement an SPNA to provide accurate S-parameter measurements for an arbitrary and reciprocal two-port network DUT over wide bandwidth at low range RF and microwave frequencies.

The theory of SPR including its designs, design criteria, and calibration techniques – were presented in this thesis, along with analysis of the chosen design, the new approach to an explicit calibration technique, and ADS simulations and reflection coefficient results to an arbitrary synthesized DUT. The simulation results confirm validity of the new approach to the explicit calibration technique.

The simulated results of the chosen design of an SPR encouraged investigation the validity of the main goal of this thesis (SPNA with independent RF power sources). Theory of operation of SPNA were presented and simulated results comparing the traditional common RF power source vs two independent RF power sources were also presented and encouraged physical realization of the chosen design/prototype.

Physical prototype of the chosen design was presented in this thesis, as well as measurement setup to confirm agreement of the manufactured PCB with the simulated circuit, and analysis of the manufacturing issues were discussed. The best results of a Low-Pass filter as DUT over wide bandwidth (approx. 0.5 GHz) were presented; however, Further work is required to confirm agreement between physical results of an SPNA with two independent

RF power sources and the simulated.

Once the physically realized SPNA results are confirmed, there is additional future work to investigate performance optimization of the chosen design. This will include de-embedding the values of S-parameters for the SPR circuit and transferring their measuring plane to the couplers (Q_2, Q_3,, and Q_4), rather than the SMAs at the power detectors and RF input power ports. Consequently, this will provide more accurate values for the physical q_i in the reflection coefficient plane, in comparison to the values for the ideal and simulated design over frequency BW. Furthermore, it will also enable closer visibility on SPR circuit behavior and sensitivity to the limitation of the connecting lines' dimensions and non-ideal behaviour of the components. Also, power detectors circuit can be developed to measure the power, rather than relying on the 24 port VNA for power measurements.

References

[1] C. A. Hoer, “The Six-Port Coupler: A New Approach to Measuring Voltage, Current, Power, Impedance and Phase,” *IEEE Trans. IM*, Vol. IM-21, 1972, pp. 466–470.

[2] G.F. Engen and C. A. Hoer, “Application of an Arbitrary 6-Port Junction to Power-Measurement Problems,” *IEEE Trans. IM*, Vol. IM-21, 1972, pp. 470–474.

[3] Keysight Technologies, “Network Analysis,” textitRF Back to Basics Seminar Presentation Material – 2018. 2018. [Online]. Available: `http://www.keysight.com/main/editorial.jspx?cc=CA&lc=eng&ckey=2782236&id=2782236&cmpid=zzfindb2bpresentations` [Accessed:Sep. 10, 2018].

[4] David M. Pozar, *Microwave Engineering*, John Wiley & Sons, Inc., 2012.

[5] R. E. Collin, *Foundations for Microwave Engineering*, 2nd edition, McGraw-Hill, New York, 2001.

[6] J. LoVetri, M. Asefi, C. Gilmore and I. Jeffrey, “Innovations in Electromagnetic Imaging Technology: The Stored-Grain-Monitoring Case”, *IEEE Antennas and Propagation Magazine*, Vol. 62, No. 5, pp. 33-42, October 2020, doi: 10.1109/MAP.2020.3003206.

[7] A. A. Olier, “Historical Perspective on Microwave Field Theory,” *IEEE Transaction on Microwave Theory and Techniques*, vol. MTT-32, pp. 1022-1045, September 1984.

[8] Keysight Technologies, “S-Parameter Measurement Basics for High Speed Digital Engineers,” *Training Material*, Jan 2014. [Online]. Available: `https://literature.cdn.keysight.com/litweb/pdf/5991-3736EN.pdf?id=2426175`

[Accessed:Sep. 22, 2018].

[9] F. Sischka.(2016, Apr 4). How to Accurately Measure and Validate S-Parameters for Transistor Modeling. Available:
`https://www.youtube.com/watch?v=f1T2-AY39C4&feature=youtu.be`
[Accessed: Sep 22, 2018]

[10] C.G. Migelez, B. Huyart, E. Bergeault, and L.P. Jaller, "A New Automobile Radar Based on the Six-Port/Frequency Discriminator," *IEEE Trans.Vehicular Tech*, Vol. 49, No.4, pp. 1416–1423, 2009.

[11] R. Mirzavand, A. Mohammadi, and A. Abdipour, "Low-Cost Implementation of Broadband Microwave Receivers in Ka Band Using Multi-Port Structures," *IET Microwaves, Antennas & Propagation,* Vol. 3, pp. 483–491, 2009.

[12] H. Wang, K. Lin, Z. Tsai, L. Lu, H. Lu, C. Wang, J. Tsai, T. Huang, and Y. Lin, "MMICs in the Millimeter-Wave Regime," *IEEE Microwave Magazine,* pp. 99–117, February 2009.

[13] F. Ghannouchi and A. Mohammadi, *The six-port technique with microwave and wireless applications.* 1st ed. Boston, MA: Artech House, 2009.

[14] G.F. Engen, "The Six-Port Reflectometer: An Alternative Network Analyzer," *IEEE Trans. on Microwave Theory and Techniques,* Vol. MTT-25, No. 12, pp. 1075–1080, Dec. 1977

[15] G. F. Engen, "An Improved Circuit for Implementing the Six-Port Technique of Microwave Measurements," *IEEE Trans. on Microwave Theory & Techniques,* Vol. MTT 25, No. 12, pp. 1080–1083, December 1977.

[16] E. J. Griffin, "Six-Port Reflectometer Circuit Comprising Three Directional Coupler," *Electron Letts.,* pp. 437–439, 1982.

[17] M. D. Rafal, and W. T. Joines, "Optimizing the Design of the Six-Port Junction," *IEEE MTT-S Digest,* pp. 437–-439, 1980.

[18] R. J. Collier and N. A. Deeb, "On the Use of a Microstrip Three Line System as a Six-Port Reflectometer," *IEEE Trans. on Microwave Theory & Techniques,* Vol. MTT-27, pp. 847–853, October 1979.

[19] A. L. Cullen, "Impedance Measurement Using Six-Port Directional Coupler," *IEE Proc.,* Vol. 127, Part H, No. 2, pp. 32–-38, April 1980.

[20] S. Julrat, M. Chongcheawchamnam, T. Khaoraphapong, and I. D. Robertson, "Analysis and Design of a Differential Sampled-Line Six-Port Reflectometer," *IEEE Trans. on Microwave Theory and Techniques.* Vol. 61, No. 1, pp. 244–255, January 2013.

[21] X.Z. Xiong and V.F. Fusco, "Wideband 0.9 GHz to 5 GHz six-port and its application as digital modulation receiver," *IEE Proc. Microwave. Antennas and Propagation.* Vol. 150, No. 4, pp. 301–307, August 2003.

[22] X.Z. Xiong, "Six-port Wireless Receiver Architectures,"Ph.D. dissertation, Dept.Elec&Elect Eng., Queen's Univ., Belfast, 2003. Accessed on: Mar 28, 2018.

[23] M. D. Rafal, and W. T. Joines, "Optimizing the Design of the Six-Port Junction," *IEEE MTT-S Digest,* pp. 437–-439, 1980.

[24] G.F. Engen, "Calibrating the Six-Port Reflectometer by Means of Sliding Terminations," *IEEE Transactions on Microwave Theory and Techniques,*Vol. MTT-26, No. 12, December 1978.

[25] T.E. Hodgetts and E.J. Griffin,"A UNIFIED TREATMENT OF THE THEORY OF SIX-PORT REFLECTOMETER CALIBRATION USING THE MINIMUM OF STANDARDS," Royal Signals and Radar Establishment, Malvern, Worcestershire., Report 83003, 1983.

[26] Ji Li, R.G. Bosisio, and Ke Wu, "Dual-Tone Calibration of Six-Port Junction and Its Application to the Six-Port Direct Digital Millimetric Receiver," *IEEE Transactions on Microwave Theory and Techniques,* Vol. 4, No. 1, pp. 93–99, January 1996.

[27] C.A. Hoer, "Using Six-Port and Eight-Port junctions to measure active and passive circuit parameters," *NBS Tech.* Note 673, September 1975.

[28] D. Wood, "Analysis and calibration theory of the general 6-port reflectometer employing four amplitude detectors," *Proc. IEE,* Vol. 126, No. 2, pp. 224–228. February 1979.

[29] S. Li and R.G. Bosisio, "Calibration of Multiport Reflectometers by Means of Four Open/Short Circuits," *IEEE Transactions on Microwave Theory and Techniques,* Vol. MTT-30, No. 7, pp. 1085–1090. July 1982.

[30] P.I. Somlo and J.D. Hunter, "A Six-Port Reflectometer and its Complete Characterization by Convenient Calibration Procedures," *IEEE Transactions and Microwave Theory and Techniques,* Vol. MTT-30, No. 2, pp. 186–192. February 1982.

[31] J.D. Hunter and P.I. Somlo,"An Explicit Six-Port Calibration Method using Five Standards," *IEEE Transactions and Microwave Theory and Techniques,* Vol. MTT-33, No. 1, pp. 69–72. January 1985.

[32] C.M. Potter and G. Hjipieris, "A Robust Six-to Four-Port Reduction Algorithm," *IEEE MTT-S Digest.,* Vol. 3, pp. 1263–1266, 1993.

[33] C.A. Hoer, "A Network Analyzer Incorporating Two Six-Port Reflectometers," *IEEE Transactions on Microwave Theory and Techniques,* Vol. MTT-25, No. 12, pp. 1070–1074, December 1977.

[34] Fadhel M. Ghannouchi and Renato G. Bosisio, "A Wideband Milimeter Wave Six-Port Reflectometer Using Four Diode Detectors Calibrated Without a Power Ratio Standard,"

IEEE Transactions on Instrumentation and Measurement, Vol. 40, No. 6, pp. 1043–1046, December 1991.

Bibliography

To support future work on the SPR circuit, I included some papers which can potentially assist in conducting the future work. Some of the following paper advertised on new structure for the preferred Engen's design for SPR and SPNA[1, and 2], as well as new design to have q_i values on the circumference of the unity circle in the reflection coefficient plane, and utilizing the spatial Fourier analysis to incorporate nonlinearity and mismatching effects as part of calibration [3]. New use of SPR to measure the moist's complex permittivity [4], as well as confirmation of designs and measurements of power for the SPR [5, and 6].

[1] Ji Jun Yao and Swee Ping Yeo, "Six-Port Reflectometer Based on Modified Hybrid Couplers," *IEEE Transactions on Microwave Theory and Techniques,* Vol. 56, No. 2, pp. 439–498, February 2008.

[2] K. Haddadi, M.M. Wang, D. Glay, and T. Lasri, "Performance of a Compact Dual Six-Port Millimeter-Wave Network Analyzer," *IEEE Transactions on Microwaver Theory and Techniques,* Vol. 60, No. 9, pp. 3207–3213, December 2011.

[3] Kamel Haddadi and Tuami Lasri, "Formulation for Complete and Accurate Calibration of Six-Port Reflectometer," *IEEE Transactions on Microwaver Theory and Techniques,* Vol. 60, No. 3, pp. 574–581, March 2012.

[4] S. Julrat and S. Trabelsi, "Portable Six-Port Reflectometer for Determining Moisture Content of Hiomass Material," *IEEE Sensors Journal,* Vol. 17, No. 15, pp. 4814–4819, 1 August 2017.

[5] K. Staszek, "Investigation on Optimum Parameter5s of Six-Port Reflectometers," *International Journal of Information and Electronics Engineering,* Vol. 9, No. 1, pp. 30–33, March 2019.

[6] K. Staszek, S. Grszczynski, and K. Wincza, "Six-Port Reflectometer Providing Enhanced Power Distribution," *IEEE Transactions on Microwave Theory and techniques,* Vol. 64, No. 3, pp. 939–951, March 2016.